AD-770 321

A STUDY OF THE FOURIER TRANSFOR METHOD OF IMAGE RESTORATION

R. S. Davidson, II

Ohio State University

Prepared for:

Rome Air Development Center
Defense Advanced Research Projects Agency

September 1973

RADC-TR-73-[illegible]
Technical Report
September 1973

AD 770321

A STUDY OF THE FOURIER TRANSFORM METHOD OF IMAGE RESTORATION

The Ohio State University

ElectroScience Laboratory

Department of Electrical Engineering
Columbus, Ohio 43212

Sponsored by
Defense Advanced Research Projects Agency
ARPA Order No. [illegible]279

Approved for public release;
distribution unlimited.

Rome Air Development Center
Air Force Systems Command
Griffiss Air Force Base, New York

UNCLASSIFIED

SECURITY CLASSIFICATION OF THIS PAGE (When Data Entered)

REPORT DOCUMENTATION PAGE

READ INSTRUCTIONS BEFORE COMPLETING FORM

1. REPORT NUMBER: RADC-TR-73-320	2. GOVT ACCESSION NO.
3. RECIPIENT'S CATALOG NUMBER	
4. TITLE (and Subtitle): A Study of the Fourier Transform Method of Image Restoration	5. TYPE OF REPORT & PERIOD COVERED: Quarterly - 1 Jan 73-31 Ja
	6. PERFORMING ORG. REPORT NUMBER: Electroscience Lab 3432-
7. AUTHOR(s): R. S. Davidson II	8. CONTRACT OR GRANT NUMBER(s): F30602-72-C-0305
9. PERFORMING ORGANIZATION NAME AND ADDRESS: Ohio State Univ Electroscience Lab, Department of Electrical Engineering, Columbus, OH	10. PROGRAM ELEMENT, PROJECT, TASK AREA & WORK UNIT NUMBERS: 62301E, 1279, 02, 05
11. CONTROLLING OFFICE NAME AND ADDRESS: Defense Advanced Research Projects Agency, Wash, DC	12. REPORT DATE: September 1973
	13. NUMBER OF PAGES: 84
14. MONITORING AGENCY NAME & ADDRESS (if different from Controlling Office): Rome Air Development Center, Environmental Studies Section (OCSE), Griffiss AFB, NY 13441	15. SECURITY CLASS. (of this report): UNCLASSIFIED
	15a. DECLASSIFICATION/DOWNGRADING SCHEDULE: N/A

16. DISTRIBUTION STATEMENT (of this Report)

Approved for public release, distribution unlimited

17. DISTRIBUTION STATEMENT (of the abstract entered in Block 20, if different from Report)

18. SUPPLEMENTARY NOTES

19. KEY WORDS (Continue on reverse side if necessary and identify by block number)

image restoration
fourier transform
restored image spectrum
image quality
poles
modulation transfer function
point spread function

20. ABSTRACT (Continue on reverse side if necessary and identify by block number)

This report examines the Fourier transform method of restoring degraded images of point objects. The principal conclusion supported by this study is that the major problem in restoring these images is the presence of poles in the restored image spectrum. A series of figures showing three restored image quality criteria graphed as functions of image degradation, for a computer modeled degraded imaging system, are presented to support this conclusion. Also included is a thorough mathematical

DD FORM 1 JAN 73 1473 EDITION OF 1 NOV 65 IS OBSOLETE

UNCLASSIFIED

SECURITY CLASSIFICATION OF THIS PAGE (When Data Entered)

A STUDY OF THE FOURIER TRANSFORM
METHOD OF IMAGE RESTORATION

R. S. Davidson II

Contractor: Ohio State University
Contract Number: F30602-72-C-0305
Effective Date of Contract: 1 April 1973
Contract Expiration Date: 30 September 1973
Amount of Contract: $75,00.00
Program Code Number: 1E20

Principal Investigator: Dr. Stuart A. Collins, Jr.
Phone: 614 422-5054

Project Engineer: Edward K. Damon
Phone: 614 422-5953

Contract Engineer: Raymond P. Urtz, Jr.
Phone: 315 330-3145

This research was supported by the Defense Advanced Research Projects Agency of the Department of Defense and was monitored by Raymond P. Urtz, Jr., RADC (OCSE), GAFB, NY 13441 under Contract F30602-72-C-0305.

PUBLICATION REVIEW

This technical report has been reviewed and is approved.

Raymond P. Urtz, Jr.

RADC Project Engineer

ACKNOWLEDGMENTS

The author would like to express his sincere thanks to his adviser, Dr. Stuart A. Collins, Jr. for his countless thoughts and suggestions contributed to this work. Acknowledgment is due, also, to Professor Edward K. Damon whose suggestions helped to improve the quality of this report.

The material contained in this report is also used as a thesis submitted to the Department of Electrical Engineering, The Ohio State University as partial fulfillment for the degree Master of Science.

ABSTRACT

This report examines the Fourier transform method of restoring degraded images of point objects. The principal conclusion supported by this study is that the major problem in restoring these images is the presence of poles in the restored image spectrum. A series of figures showing three restored image quality criteria graphed as functions of image degradation, for a computer modeled degraded imaging system, are presented to support this conclusion. Also included is a thorough mathematical analysis of the restored image spectrum.

TABLE OF CONTENTS

CHAPTER I
INTRODUCTION

A. Statement of the Problem

We know that atmospheric turbulence degrades the images of objects that are recorded by optical systems. Mirages and star twinkling are typical examples. It is important for some applications that we be able to extract as much information as possible from these degraded images concerning the actual object especially in cases where this object is an unknown quantity. Because the human visual system is an inefficient processor of this data, it is necessary to resort to other processing techniques. Out of this need for more efficient processing techniques emerges the study of image restoration.

The goal of this study is to specify the limits over which one such processing technique, the Fourier transform method, does restore a turbulence degraded image so that it is a more accurate representation of the actual object. For this study, we will model a turbulence degraded imaging system, and apply the Fourier transform processing technique to the resulting degraded images to determine the actual object.

B. Background Discussion of Imaging in the Presence of Atmospheric Turbulence

Objects which are imaged through the atmosphere are degraded as a result of random temperature fluctuations in that atmosphere. In this section a brief discussion of these degrading effects is presented.

Imaging through a turbulent atmosphere is not a new phenomena, for man's own imaging system, the eye, has always had to contend with this problem whenever a temperature gradient was present along his line of sight. One of the most familiar instances today of the eye imaging through a turbulent atmosphere occurs while driving along a highway which is reradiating solar energy. As one looks at a car or the scenery some distance ahead, the objects seem to be dancing and are blurred because of the atmospheric effects. In this case the phenomena is commonly referred to by the phrase "the heat is rising".

The atmosphere is a gas and thus as it is warmed, its density, and hence its index of refraction, changes. The warmer layers rise and mix with the cooler and more dense layers which are falling due to gravitational forces. This mixing causes additional refractive index changes to occur. These changes are referred to as refractive index fluctuations and are obviously random functions of time which are best described by statistical means. (See Tatarski [1,2].)

A light wave propagating through a non-turbulent atmosphere is focused by a telescope to a specific point in the image plane. However, when the propagation path contains refractive index fluctuations one may consider effects occuring on two spatial scales which degrade the ideal imaging situation. First, for those refractive index fluctuations which vary slowly over a spatial scale larger than the telescope input aperture, the image plane effect is similar to that which occurs when a prism is placed in front of the telescope input aperture. That is, the incoming rays are bent causing the focused image to be shifted to a new image plane coordinate location. Second, for those refractive index fluctuations which vary rapidly over a spatial scale comparable to the input aperture, the result observed in the optical system image plane is that of image break-up.

Both of these effects obviously perturb the incoming wave phase fronts. By including a random time variation in these phase front perturbations, the resulting image plane pattern is a "dancing", blurred and broken-up corruption of the ideal image.

C. Mathematical Concepts and the Fourier Transform Method of Image Restoration

The familiar one-dimensional mathematical concepts of the convolution integral and the Fourier transform pair are extended to a two-dimensional generalization. These two-dimensional generalizations form the mathematical foundation on which the Fourier transform method of image restoration is based.

First, consider the extension of one-dimensional linear system theory, commonly associated with electrical engineering, to the two-dimensional linear imaging system. It has been shown (see Goodman [3]) that the image plane intensity function and the object plane intensity function for an incoherent object are related by a convolution integral of the form:

$$(1) \qquad I_i(x_2,y_2) = \iint_{-\infty}^{\infty} h(x_2-x_1,y_2-y_1)\, I_0(x_1,y_1)\, dx_1\, dy_1 \quad ,$$

where $I_i(x_2,y_2)$ and $I_0(x_1,y_1)$ are the image and object plane intensity functions, respectively. This integral should be recognized as the extension to two dimensions of the one-dimensional integral familiar to all electrical engineers, which relates the output and input of a linear system. As in linear network theory, the two-dimensional generalization has associated with it a unit impulse response $h(x_2,y_2)$. This impulse response is obtained by placing an intensity point source in the object

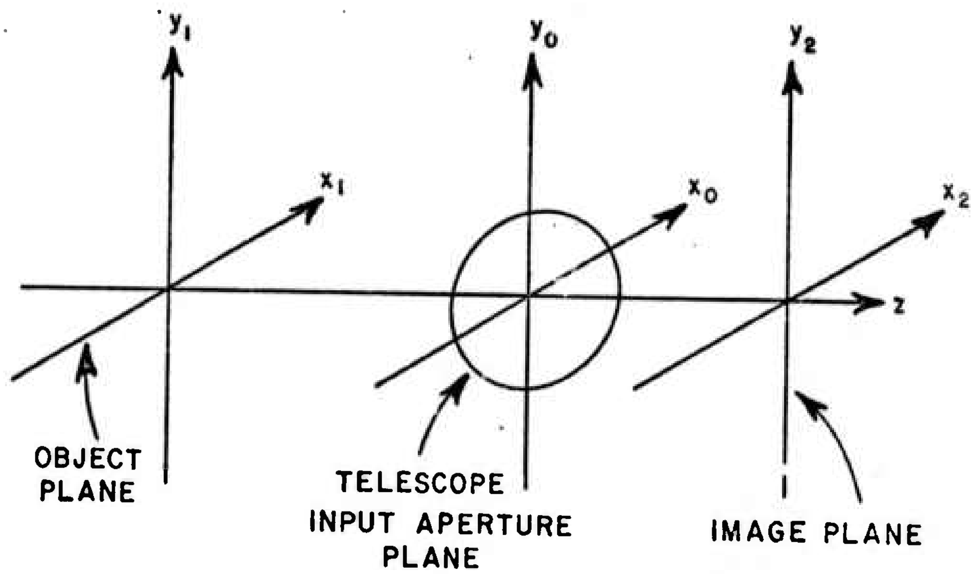

Fig. 1. Imaging coordinate systems.

plane. This impulse response is referred to as the intensity point spread function (PSF) and is defined as:

$$(2) \qquad I_i(x_2,y_2) = h(x_2,y_2) = \iint_{-\infty}^{\infty} h(x_2-x_1,y_2-y_1)\ \delta(x_1,y_1)\ dx_1\ dy_1$$

where $\delta(x_1,y_1)$ is a two-dimensional Dirac delta function.

The integral in Eq. (1) is valid only over that portion of the object plane for which $h(x_2,y_2)$ is independent of the location of $\delta(x_1,y_1)$. This region over which the integral is said to be spatially invariant is known as an isoplanatic patch and is analogous to the time invariance condition in electrical circuits.

Defining a two-dimensional generalization of the Fourier transform pair as:

$$(3) \qquad f(x,y) \leftrightarrow F(K_x,K_y) \quad ,$$

where the symbol $\leftrightarrow$ indicates that the two functions are Fourier transform mates, we have:

$$(4) \qquad F(K_x,K_y) = \iint_{-\infty}^{\infty} f(x,y)\, e^{-j(K_x x + K_y y)}\, dx\, dy$$

and

$$(5) \qquad f(x,y) = \frac{1}{(2\pi)^2} \iint_{-\infty}^{\infty} F(K_x,K_y)\, e^{j(K_x x + K_y y)}\, dK_x\, dK_y \quad .$$

In Eqs. (4) and (5), K_x and K_y are defined as spatial frequencies with the dimensions of radians/mm. Applying this generalized Fourier transform to Eq. (1), we see from the convolution theorem that:

$$(6a) \qquad I_i(K_x,K_y) = H(K_x,K_y)\, I_0(K_x,K_y) \quad .$$

The function $H(K_x,K_y)$ is known as the system modulation transfer function (MTF) and is analogous to the network transfer function used in linear circuit theory. The functions $I_i(K_x,K_y)$ and $I_0(K_x,K_y)$ are the spatial spectra of the image and object plane intensity functions, respectively.

The recorded image plane intensity will be a degraded form of $I_0(x_1,y_1)$, the object intensity function, if the region between the object plane and the telescope input aperture is assumed to be a turbulent medium. However, we can obtain the MTF of the system, including the turbulence effects, by placing a point source in the same isoplanatic patch occupied by $I_0(x_1,y_1)$. The input intensity function $I_0(x_1,y_1)$ can then be determined by dividing the degraded image plane intensity function spectrum by the system MTF (the quotient

$$(6b) \qquad I_0(K_x,K_y) = \frac{I_i(K_x,K_y)}{H(K_x,K_y)}$$

is defined as the restored image spectrum (RIS)) and taking the inverse Fourier Transform of this RIS. The result of these operations is the restored image, which is:

$$(7) \qquad I_R(x_1,y_1) = I_0(x_1,y_1) = \frac{1}{(2\pi)^2} \iint_{-\infty}^{\infty} I_0(K_x,K_y)\, e^{j(K_x x + K_y y)}\, dK_x\, dK_y$$

$$= \frac{1}{(2\pi)^2} \iint_{-\infty}^{\infty} \frac{I_i(K_x,K_y)}{H(K_x,K_y)}\, e^{j(K_x x + K_y y)}\, dK_x\, dK_y$$

where $I_R(x_1,y_1)$ is defined as the restored image.

For a randomly varying turbulent medium, an isoplanatic region, which was defined earlier as the region over which Eq. (1) is spatially invariant, is not defined by sharp boundaries but rather by more smoothly varying transitions. As the separation between the object and the point source increases, the phase front perturbations across the telescope input aperture become different since the beams have propagated along paths having slightly different small and large scale refractive index fluctuations. Thus, one would expect that as the reference point source is moved through such transition regions, the quality of the restored image would decrease to the point where it cannot be considered as a valid restored image.

D. Summary of Image Restoration Methods

In the past, there have been various methods suggested for the restoration of turbulence degraded images. Among these schemes have been wavefront reconstruction (Gaskill [4], Goodman [5]); maximum likelihood restoration (Frieden [6]); spatial filtering (Mueller [7], Reynolds [7]); constrained deconvolution (MacAdams [8]); and the Fourier transform method (Harris [9], McGlamery [10]). These and other methods have been applied to restoring image degradation resulting from effects other than atmospheric turbulence, such as image motion or optical and electrical degradation (Huang [11], Andrews [12], Sawchuk [13]).

This present study is concerned with the Fourier transform method as it applies to the restoration of turbulence-degraded images. It should be pointed out, however, that this method is also applicable to some of the other sources of image degradation such as image motion.

The previous work involving the Fourier transform restoration scheme has been qualitative in nature. It has demonstrated this method using artificially generated or computer modelled image degrading effects. In this study we emphasize the quantitative aspects of the restored image quality obtained using the Fourier transform method. The image quality is presented as a function of deviations from the ideal PSF which yields the perfectly restored image.

The question we attempt to answer in this study is, how large may these deviations become before the Fourier transform method fails to produce good image restoration results? The results obtained from answering this question may serve as the input data needed to answer other imaging questions such as, what is the isoplanatic patch size of a turbulent atmosphere?

E. Organization of the Study

In Chapter I, we have discussed the image degrading effects of a turbulent atmosphere. We have described a typical imaging system and presented the necessary mathematical background required to apply the

Fourier transform method of image restoration to a turbulence degraded image.

In Chapter II, we generate a mathematical model that describes the turbulence degraded wavefronts across the input aperture of the imaging system as a polynomial series. Using this model we then derive an equation for the restored image spectrum (RIS). The actual restored image obtained by using the Fourier transform method can then be determined by calculating the inverse Fourier transform of this RIS. The discrete form of this RIS is also presented in this chapter. It is this discrete equation that is programmed on a digital computer which calculates the inverse Fourier transform (yielding the restored image) for various model parameters.

In Chapter III we first define what is meant by the phrase "an ideally restored image". Based on this definition we then note that the presence of poles in the RIS may cause the inverse Fourier transform of the RIS to be a very poorly restored image. As a result, we then conduct an extensive analysis of the RIS and its poles, the outcome being a series of equations relating the number of poles and their positions to the degraded wavefront model parameters. These equations serve as input data for a quantitative analysis of restored image quality versus RIS pole position and number. Finally, in Chapter III we define the parameters that we will use to describe the quality of a restored image.

In Chapter IV, quantitative results of restored image quality are presented as a function of the degraded wavefront model parameters. Three cases are thoroughly examined that relate these model parameters to specifically known RIS pole placement and number; the result is the definition of regions of successful image restoration separated by regions characterized by gross departures from the restored image quality criterion. A series of graphs is included for each case showing the regions of successful and unsuccessful image restoration.

Chapter V is devoted to a summary of the entire study. Also, a series of conclusions are drawn relating the results of this study to the task of restoring turbulence degraded images.

F. Summary

The goal of this study, as stated previously, is to determine the limits over which the Fourier transform method of image restoration does indeed produce a valid representation of the actual input object. A secondary goal is to specify these limits in such a manner that they may serve as input data for a future study relating the restored image quality to the isoplanatic patch size.

CHAPTER II
CALCULATION OF THE RESTORED IMAGE SPECTRUM

A. Introduction

In Chapter I we briefly described the degrading effects of the large and small scale index fluctuations on an imaging system. We also indicated that the Fourier transform method will be the approach used in this study to restore such turbulence degraded images.

In this chapter, we turn our attention to a more detailed mathematical model of the imaging system from which the restored image spectrum (RIS) is calculated in terms of phase front parameters. The incoming turbulence degraded optical phase front will be expanded in terms of a general second degree quadratic equation. Using this expansion we then calculate the restored image spectrum for both continuous and discrete values of the spatial frequencies K_x and K_y. These results will be used in Chapter III where we thoroughly examine the RIS.

B. The Imaging System Model

This imaging system model discussion is divided into two sections. First, the physical layout and coordinate system used are described. Second, the expansion for the turbulence degraded input electric fields (E fields) is derived.

We choose the coordinate system in Fig. 2 for the imaging system.

The (x_0,y_0) plane contains the telescope input aperture which is assumed to be square, with width $W = 2x_m = 2y_m$. This assumption simplifies the mathematics but does not detract from the fundamental results.

The (x_1,y_1) object plane is located a distance d_0 from the input aperture and contains the reference point source and the object that we are imaging. The medium separating these two planes is assumed to be a turbulent atmosphere having randomly varying refractive index fluctuations. The (x_2,y_2) plane is located a distance d_i from the input aperture and is the image plane of the telescope. The distances d_0 and d_i are conjugate distances since we are considering an imaging situation. The region between the (x_0,y_0) and (x_2,y_2) planes is assumed to be void of any turbulent effects.

Both the reference source and the object are assumed to be monochromatic point sources which are described mathematically by the two-dimensional Dirac delta function. The separation between these two points is the distance d_s. The imaging system is assumed to be linear,

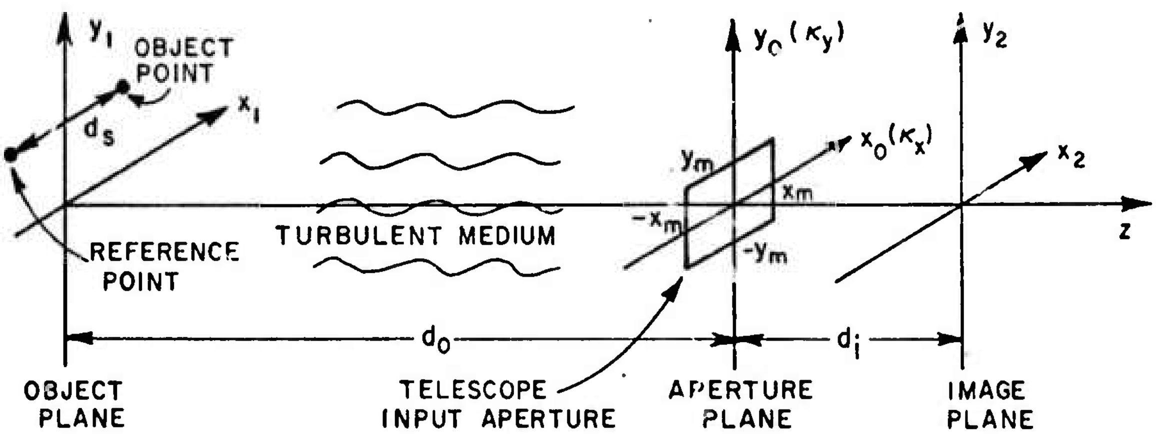

Fig. 2. Coordinate system for imaging system model.

thus, analysis of an extended object would require integration of the point object results over all points in the extended object.

The field distribution over the input aperture, for a point object located at a finite distance d_0 and in the absence of turbulence, is merely a spherical wave having uniform phase. However, in the presence of turbulence and assuming negligible amplitude effects, we use Frieds [14] assumption that the perturbed E-field phase fronts may be described by a general second degree quadratic equation involving x_0 and y_0. That is, the instantaneous phase ϕ may be expanded in the form:

$$\phi = ax_0^2 + bx_0y_0 + cy_0^2 + dx_0 + ey_0 + f \quad . \tag{8a}$$

This formulation can represent any wavefront that involves spherical and hyperbolic perturbations, wavefront tilt and an average phase term.

An alternative representation for the instantaneous phase ϕ which clearly defines these distortions is the polynomial series used by Collins [15].

$$\phi = \sum_{n=1}^{6} a_n' \, F_n(x_0,y_0) \tag{8b}$$

where:

$$F_1(x_0,y_0) = \frac{1}{W}$$

$$F_2(x_0,y_0) = \frac{\sqrt{3}}{W}\frac{x_0}{W/2}$$

$$F_3(x_0,y_0) = \frac{\sqrt{3}}{W}\frac{y_0}{W/2}$$

$$F_4(x_0,y_0) = \frac{1}{W}\frac{3}{2}\sqrt{\frac{5}{2}}\left(x_0{}^2 + y_0{}^2 - \frac{W^2}{6}\right) / (W/2)^2$$

$$F_5(x_0,y_0) = \frac{1}{W}\frac{3}{2}\sqrt{\frac{5}{2}}(x_0{}^2 - y_0{}^2) / (W/2)^2$$

$$F_6(x_0,y_0) = \frac{3}{W}\, x_0 y_0 / (W/2)^2 \quad .$$

Each polynomial has a particular interpretation. $F_1(x_0,y_0)$ represents a constant phase contribution; $F_2(x_0,y_0)$ and $F_3(x_0,y_0)$ represent tilts in the x_0 and y_0 directions respectively; $F_4(x_0,y_0)$ represents a spherical distortion; and $F_5(x_0,y_0)$ and $F_6(x_0,y_0)$ represent hyperbolic distortions. These functions are chosen to be orthonormal over a square of width W. The coefficients a, b, c, d, e, and f in Eq. (8a) are related to the coefficients a_1', a_2', a_3', a_4', a_5' and a_6' by the following equations in which

$$C_W = \frac{1}{W}\frac{3}{2}\sqrt{\frac{5}{2}}\frac{1}{(W/2)^2} \quad .$$

$$a = \frac{1}{W}\frac{3}{2}\sqrt{\frac{5}{2}}\frac{1}{(W/2)^2}(a_4' + a_5') = C_W(a_4' + a_5')$$

$$b = \frac{1}{W}\frac{3}{(W/2)^2}a_6'$$

$$c = \frac{1}{W}\frac{3}{2}\sqrt{\frac{5}{2}}\frac{1}{(W/2)^2}(a_4' - a_5') = C_W(a_4' - a_5')$$

$$d = \frac{1}{W/2}\frac{\sqrt{3}}{W}a_2'$$

$$e = \frac{1}{W/2} \frac{\sqrt{3}}{W} a_3'$$

$$f = \frac{a_1'}{W} - \sqrt{\frac{5}{2}} \frac{a_4'}{W}$$

The representation given in Eq. (8a) will be used extensively throughout the remainder of this study because of its computational simplicity, although the results in Chapter IV are given in terms of both sets of coefficients to facilitate interpretation in light of other work using the Eq. (8b) expansion. Thus, using the expansion in Eq. (8a) the turbulence degraded field distribution over the aperture plane resulting from a point object may be expressed as:

$$(9) \qquad E_a(x_0,y_0) = e^{j(ax_0^2 + bx_0y_0 + cy_0^2 + dx_0 + ey_0 + f)} .$$

This E-field distribution is the general form assumed for the imaging system model.

In the field of optics, it is a well known fact (see Goodman [3]) that when a lens system images an object, the field distribution over the input aperture and the field distribution over the image plane differ by a constant term and a phase term from being exact Fourier transform mates. This relationship is expressed as:

$$(10) \qquad E_i(x_2,y_2) = \frac{A}{(2\pi)^2}\left(\frac{k}{d_i}\right)^2 e^{j\xi} \iint_{-\infty}^{\infty} E_a(x_0,y_0) e^{j(k/d_i)(x_0x_2+y_0y_2)} dx_0\, dy_0$$

where $E_a(x_0,y_0)$ and $E_i(x_2,y_2)$ are the aperture and image plane field distributions respectively.

If we define the spatial frequencies as:

$$(11a) \qquad K_x \stackrel{\Delta}{=} \frac{kx_0}{d_i}$$

and

$$(11b) \qquad K_y \stackrel{\Delta}{=} \frac{ky_0}{d_i} .$$

then the more familiar Fourier transform expression is obtained.

$$(12) \qquad E_i(x_2,y_2) = \Lambda\, e^{i\phi} \frac{1}{(2\pi)^2} \iint_{-\infty}^{\infty} E_a(K_x,K_y) e^{j(K_x x_2 + K_y y_2)}\, dK_x\, dK_y \quad .$$

By substituting the above definition of spatial frequencies into Eq. (9), the aperture plane E-field distribution becomes:

$$(13) \qquad E_a(K_x,K_y) = e^{j\left[(d_i/k)^2(aK_x^2+bK_xK_y+cK_y^2) + (d_i/k)(dK_x+eK_y) + f\right]} \quad .$$

In this study, where we are interested in the instantaneous value of the E-field in Eq. (13), we choose not to include the wavefront tilt terms (the d and e terms) and the average phase term (the f term) in the analysis of the point object. The wavefront tilt terms merely shift the image to a different coordinate location but, for short exposures, do not actually degrade the image detail (recall the time shifting property in one-dimensional Fourier transform theory). The constant phase term is merely a multiplicative factor that drops out anyway when the intensities are calculated. Thus, the actual field distribution assumed for the imaging system model is:

$$(14) \qquad E_a(K_x,K_y) = e^{j\left[(d_i/k)^2(aK_x^2 + bK_xK_y + cK_y^2)\right]} \quad .$$

The parameters a, b and c are defined as:

$$(15a) \qquad a \triangleq 2\pi a_1/(W/2)^2 = 2\pi a_1/x_m^2$$

$$(15b) \qquad b \triangleq 2\pi b_i/(W/2)^2 = 2\pi b_1/x_m y_m$$

$$(15c) \qquad c \triangleq 2\pi c_1/(W/2)^2 = 2\pi c_1/y_m^2$$

where a_1, b_1 and c_1 specify the amount of wavefront distortion, in fractions of a wavefront, at the edge of the input aperture. Furthermore, since the input aperture is now considered a spatial frequency plane, the aperture dimensions define the system E-field spatial frequency band limit K_m to be:

$$(16) \qquad K_m = \frac{k}{d_i} x_m = \frac{k}{d_i} y_m = \frac{k}{d_i}\frac{W}{2} \quad .$$

Remember that the aperture has been assumed to be square with width $W = 2x_m = 2y_m$.

C. The Continuous Restored Image Spectrum

Using the model discussed in section B and the degraded aperture plane E-field given in Eq. (14), the restored image spectrum (RIS) is next calculated.

The first step toward finding the RIS is the calculation of the image plane intensity function and its spectrum in terms of the E-field given in Eq. (14). This image plane intensity function is

$$I(x_2,y_2) = E_i(x_2,y_2)\, E_i^*(x_2,y_2) \tag{17}$$

where the * notation indicates the complex conjugate of the function. (Note that Z_0, the impedance of free space, has been dropped. It is merely a multiplicative constant that would be cancelled in later steps where ratios of intensities are formed.) $E_i(x_2,y_2)$ is given by:

$$E_i(x_2,y_2) = \frac{Ae^{i\xi}}{(2\pi)^2} \iint_{-\infty}^{\infty} W(K_x,K_y)\, E_a(K_x,K_y)\, e^{j(K_x x_2 + K_y y_2)}\, dK_x\, dK_y \tag{18}$$

where $W(K_x,K_y)$ is the aperture function which takes into account the finite sized input aperture. The function $W(K_x,K_y)$ is defined as:

$$W(K_x,K_y) = \begin{cases} 1 & \begin{array}{l} -K_m \le K_x \le K_m \\ -K_m \le K_y \le K_m \end{array} \\ 0 & \text{otherwise} \end{cases} \tag{19}$$

From Fourier transform theory we know that if:

$$E_i(x_2,y_2) \leftrightarrow E_a(K_x,K_y)$$

then

$$E_i^*(x_2,y_2) \leftrightarrow E_a^*(-K_x,-K_y) \quad ,$$

and, additionally, that multiplication in the spatial plane is equivalent to convolution in the spatial frequency plane. Using these facts, the image plane intensity is found to be the Fourier transform of the convolution integral given in Eq. (20) below.

$$(20)\qquad I(x_2,y_2) = E_i(x_2,y_2)\,E_i^*(x_2,y_2) \longleftrightarrow$$

$$\frac{1}{(2\pi)^2}\iint_{-\infty}^{\infty} W(K_x-k_x,K_y-k_y)\,W^*(-k_x,-k_y)$$

$$E_a(K_x-k_x,K_y-k_y)\,E_a^*(-k_x,-k_y)\,dk_x\,dk_y \quad .$$

The variables k_x and k_y are dummy variables that have the dimensions of spatial frequency.

By letting $k_x = -k_x$ and $k_y = -k_y$ and multiplying Eq. (20) by $(2\pi)^2$, we define the image plane function $I_i(x_2,y_2)$ as:

$$(21)\qquad I_i(x_2,y_2) = (2\pi)^2 I(x_2,y_2) \leftrightarrow I_i(K_x,K_y) = C(K_x,K_y) =$$

$$\iint_{-\infty}^{\infty} W(K_x+k_x,K_y+k_y)\,W^*(k_x,k_y)$$

$$E_a(K_x+k_x,K_y+k_y)\,E_a^*(k_x,k_y)\,dk_x\,dk_y$$

where $I_i(K_x,K_y)$ is the spatial frequency spectrum of $I_i(x_2,y_2)$. The integral in Eq. (21) has the form of a correlation function and hence is referred to as the aperture plane correlation function, which is defined as $C(K_x,K_y)$.

Substituting Eq. (14) into Eq. (21), we have:

$$(22)\qquad I_i(x_2,y_2) \leftrightarrow C(K_x,K_y) = \iint_{-\infty}^{\infty} W(K_x+k_x,K_y+k_y)\,W^*(k_x,k_y)$$

$$e^{j(d_i/k)^2\left[a(K_x+k_x)^2 + b(K_x+k_x)(K_y+k_y) + c(K_y+k_y)^2\right]}$$

$$e^{j(d_i/k)^2\left[ak_x^2 + bk_xk_y + ck_y^2\right]}\,dk_x\,dk_y \quad .$$

When the phase term involving only K_x and K_y is brought outside the integral, we have:

$$(23)\qquad I_i(x_2,y_2) \leftrightarrow C(K_x,K_y) = e^{j(d_i/k)^2(aK_x{}^2 + bK_xK_y + cK_y{}^2)}$$

$$\iint_{-\infty}^{\infty} W(K_x+k_x,K_y+k_y)\, W^*(k_x,k_y)\, e^{j(d_i/k)^2\left[(2aK_x+bK_y)k_x+(2cK_y+bK_x)k_y\right]}$$

$$dk_x\, dk_y \; .$$

The details of evaluating the above integral are carried out in Appendix A. The final result of this calculation is presented below.

$$(24)\qquad I_i(x_2,y_2) \leftrightarrow C(K_x,K_y) =$$

$$(2K_m - |K_x|)\left[\frac{\operatorname{Sin}\{(d_i/k)^2(2aK_x+bK_y)\tfrac{1}{2}(2K_m-|K_x|)\}}{(d_i/k)^2(2aK_x+bK_y)\tfrac{1}{2}(2K_m-|K_x|)}\right]$$

$$\cdot\,(2K_m - |K_y|)\left[\frac{\operatorname{Sin}\{(d_i/k)^2(2cK_y+bK_x)\tfrac{1}{2}(2K_m-|K_y|)\}}{(d_i/k)^2(2cK_y+bK_x)\tfrac{1}{2}(2K_m-|K_y|)}\right] \; .$$

Note that $C(K_x,K_y)$, being the transform of an image intensity function, has a spatial frequency bandwidth twice that of the image plane E-field given in Eq. (16). The region over which $C(K_x,K_y)$ is defined is:

$$-2K_m \le K_x \le 2K_m$$

$$-2K_m \le K_y \le 2K_m \; .$$

Eq. (24) is the product of two triangular functions $(2K_m - |K_x|)$ and $(2K_m - |K_y|)$ each of which is modulated by a function having a Sin x/x format (commonly referred to as a Sinc function). The degrading effects of the atmospheric turbulence, as represented by the parameters a, b, and c, are introduced through the arguments of the Sinc functions. Note that when a = b = c = 0 (i.e., in the absence of turbulence), the correlation function is:

$$(25)\qquad C(K_x,K_y) = (2K_m - |K_x|)\,(2K_m - |K_y|) \; .$$

This function is the two-dimensional generalization of the familiar correlation of two one-dimensional rectangular pulses. For the two-dimensional case, Eq. (25) is the correlation of the aperture function $W(K_x, K_y)$ with itself.

The reference source is also a point source; thus, Eq. (14) also describes the resulting aperture phase distribution when there is zero separation ($d_s = 0$) between the reference point and object point. However, for finite separations between these two points, the atmospheric effects on the waves radiating from the two points will, in general, be different. These differences are incorporated in the aperture plane expansion for the reference E-field by defining the reference phase parameters as:

(26a) $$a_o = a + \Delta a$$

(26b) $$b_o = b + \Delta b$$

(26c) $$c_o = c + \Delta c$$

where Δa, Δb, and Δc represent small perturbations in the parameters a, b, and c, which describe the aperture plane E-field for the point object.

The reference point aperture plane field distribution is obtained by substituting Eqs. (26a), (26b), and (26c) into Eq. (14) to obtain:

(27) $$E_a(K_x, K_y) = e^{j(d_i/k)^2 (a_o K_x^2 + b_o K_x K_y + c_o K_y^2)}$$

$$= e^{j(d_i/k)^2 \left((a+\Delta a)K_x^2 + (b+\Delta b)K_x K_y + (c+\Delta c)K_y^2\right)} .$$

The modulation transfer function (MTF) is the system transfer function obtained when the reference input is a point source (see Chapter I). Actually we have already derived this function in Eq. (24) where the object was also assumed to be a point source. Thus the MTF is obtained by substituting Eqs. (26a), (26b), and (26c) into Eq. (24). Remember that the resulting function is the Fourier transform of the system PSF (see Chapter I). The MTF is:

$$(28)\qquad H(K_x,K_y)=(2K_m-|K_x|)\left[\frac{\mathrm{Sin}\{(d_i/k)^2(2\left[(a+\Delta a)K_x+(b+\Delta b)K_y\right]\tfrac{1}{2}(2K_m-|K_x|)\}}{(d_i/k)^2(2\left[(a+\Delta a)K_x+(b+\Delta b)K_y\right]\tfrac{1}{2}(2K_m-|K_x|)}\right]$$

$$\cdot(2K_m-|K_y|)\left[\frac{\mathrm{Sin}\{(d_i/k)^2(2\left[(c+\Delta c)K_y+(b+\Delta b)K_x\right]\tfrac{1}{2}(2K_m-|K_y|)\}}{(d_i/k)^2(2\left[(c+\Delta c)K_y+(b+\Delta b)K_x\right]\tfrac{1}{2}(2K_m-|K_y|)}\right]$$

We now have calculated the spectrum for the image plane intensity, the aperture plane correlation function (Eq. (24)), and we have also calculated the MTF which is the transform of the PSF. Next, we will use the MTF and the degraded image spectrum to calculate the restored image spectrum (RIS) $I_R(K_x,K_y)$ using the approach given in Eq. (7).

$$(29)\qquad I_R(K_x,K_y) = \frac{I_i(K_x,K_y)}{H(K_x,K_y)} = \frac{C(K_x,K_y)}{H(K_x,K_y)} \quad .$$

Substituting Eqs. (15a), (15b) and (15c) into Eqs. (24) and (28) and performing the division indicated in Eq. (29), the restored image spectrum is calculated in terms of K_x and K_y, the spatial frequency components; a_1, b_1 and c_1, the object phase front parameters; and Δa_1, Δb_1 and Δc_1, the reference phase perturbation parameters. The notation used for this RIS given below has been chosen to emphasize the eight independent variables discussed above. The notation to be used is:

$$(30)\qquad I_R(K_x,K_y) = R(K_x,K_y,a_1,b_1,c_1,\Delta a_1,\Delta b_1,\Delta c_1) \quad .$$

Actual calculation of the RIS is straightforward but tedious; thus, it is carried out in Appendix B. The result of this calculation is that the RIS has the mathematical form:

$$(31)\qquad R(K_x,K_y,a_1,b_1,c_1,\Delta a_1,\Delta b_1,\Delta c_1) = \left[1 + \frac{2\Delta a_1K_x + \Delta b_1K_y}{2a_1K_x + b_1K_y}\right]$$

$$\Big[\mathrm{Cos}\left\{(2\pi/K_m^2)\tfrac{1}{2}(2K_m-|K_x|)(2\Delta a_1K_x+\Delta b_1K_y)\right\}$$

$$-\mathrm{Sin}\left\{(2\pi/K_m^2)\tfrac{1}{2}(2K_m-|K_x|)(2\Delta a_1K_x+\Delta b_1K_y)\right\}\cdot\mathrm{Cot}\Big\{(2\pi/K_m^2)\tfrac{1}{2}(2K_m-|K_x|)$$

$$\cdot(2(a_1+\Delta a_1)K_x+(b_1+\Delta b_1)K_y)\Big\}\Big]\left[1 + \frac{2\Delta c_1K_y + \Delta b_1K_x}{2c_1K_y + b_1K_x}\right]$$

$$\cdot\left[\mathrm{Cos}\left\{(2\pi/K_m^2)^{\frac{1}{2}}(2K_m-|K_y|)(2\Delta c_1K_y + \Delta b_1K_x)\right\} - \mathrm{Sin}\left\{(2\pi/K_m^2)\right.\right.$$

$$\left.\cdot\tfrac{1}{2}(2K_m-|K_y|)(2\Delta c_1K_y + \Delta b_1K_x)\right\}\mathrm{Cot}\left\{(2\pi/K_m^2)^{\frac{1}{2}}(2K_m-|K_y|)\right.$$

$$\left.\left.\cdot(2(c_1+\Delta c_1)K_y + (b_1+\Delta b_1)K_x)\right\}\right] \quad .$$

For small values of Δa_1, Δb_1 and Δc_1 (i.e., much less than 1.0), Eq. (31) may be simplified by using the small argument approximations for the Sin and Cos functions. That is, for small values of the arguments, we have:

$$\mathrm{Sin}\ \alpha \approx \alpha$$

$$\mathrm{Cos}\ \alpha \approx 1$$

where α may be the argument of any Sin or Cos term in Eq. (31). Using these approximations, Eq. (31) is greatly simplified and may be rewritten as:

$$(32) \qquad R(K_x,K_y,a_1,b_1,c_1,\Delta a_1,\Delta b_1,\Delta c_1) = \left[1 + \frac{2\Delta a_1K_x + \Delta b_1K_y}{2a_1K_x + b_1K_y}\right]$$

$$\cdot\left[1 - \left\{(2\pi/K_m^2)^{\frac{1}{2}}(2K_m-|K_x|)(2\Delta a_1K_x+\Delta b_1K_y)\right\}\mathrm{Cot}\left\{(2\pi/K_m^2)^{\frac{1}{2}}(2K_m-|K_x|)\right.\right.$$

$$\left.\left.\cdot(2(a_1+\Delta a_1)K_x + (b_1+\Delta b_1)K_y)\right\}\right]\left[1 + \frac{2\Delta c_1K_y + \Delta b_1K_x}{2c_1K_y + b_1K_x}\right]$$

$$\cdot\left[1 - \left\{(2\pi/K_m^2)^{\frac{1}{2}}(2K_m-|K_y|)(2\Delta c_1K_y+\Delta b_1K_x)\right\}\mathrm{Cot}\left\{(2\pi/K_m^2)^{\frac{1}{2}}(2K_m-|K_y|)\right.\right.$$

$$\left.\left.\cdot(2(c_1+\Delta c_1)K_y + (b_1+\Delta b_1)K_x\right\}\right] \quad .$$

At this point we have a mathematical relationship which describes the RIS in terms of the parameters a_1, b_1, c_1, Δa_1, Δb_1, and Δc_1 which are associated with the turbulence-induced effects. This expression is used in the next section of this chapter where the discrete form for the RIS is derived; it is also used in Chapter III where a thorough analysis of the RIS is conducted.

D. The Discrete Restored Image Spectrum

The expression given in Eq. (32) describes the restored image spectrum as a continuous function; however, restoration techniques employing digital computers require only a finite number of data samples, taken in compliance with the Nyquist sampling criterion, to describe a band-limited function. Since we are interested in computer processing of turbulence degraded images, we now proceed to derive the discrete form of Eq. (32) which we assume to be a valid representation for the RIS.

The discrete RIS for an actual imaging system would be obtained by sampling the degraded image and the PSF in the telescope image plane. The resulting two sampled data arrays are then read into a digital computer where their Fourier transforms are calculated using a fast Fourier transform (FFT) algorithm. (See Appendix C for a discussion of the FFT.) The ratio of the two discrete transforms (i.e., image spectrum divided by MTF) yields the discrete RIS.

The sample spacing used in the image plane and the quantitized spatial frequencies are next calculated. In Eq. (24) the spatial frequency band limit for the image intensity was found to be $2K_m$. For this study we assume that the images are sampled with 64 x 64 sample resolution. Thus, in accordance with Nyquist's criterion, the sample spacing must be:

(33a) $$\Delta x_2 = \Delta y_2 \leq \pi/2K_m$$

for which the quantitized spatial frequency is:

(33b) $$\Delta K_x = \Delta K_y = 4K_m/64 = 2\pi/64\Delta x_2 = 2\pi/64\Delta y$$

(See Appendix C for details).

It is assumed for the model used here that a telescope input aperture actually limits the frequency content of the intensity functions to $63\Delta K_x$ and $63\Delta K_y$ (i.e., $64\Delta K_x = 64\Delta K_y = 0$); however, the image plane functions are sampled with 64 x 64 resolution. Thus, the image is sampled at greater than the Nyquist rate, which eliminates the problem of aliasing in the spectrum.

We are now equipped to calculate the discrete RIS from Eq. (32) by making the substitutions:

(34a) $$K_x \rightarrow p\Delta K_x$$

(34b) $$K_y \rightarrow q\Delta K_y$$

where p and q = 0, ±1,2,··· 31 and ΔK_x and ΔK_y are the discrete spatial frequencies given in Eq. (33b).

In terms of the "R" function notation introduced in Eq. (30), the discrete RIS is given in Eq. (35) below.

(35) $$\text{Discrete RIS} = R(p\,\Delta K_x,\ q\,\Delta K_y,\ a_1, b_1, c_1, \Delta a_1, \Delta b_1, \Delta c_1)$$

The restored image is obtained by taking the inverse FFT of the function given in Eq. (35). It is the quality of this resulting restored image that we discuss in Chapter IV.

It is worthwhile to show the relationship between the discrete frequencies in the RIS passband and K_m, the input aperture halfwidth, where this halfwidth is expressed in units of spatial frequency (see Eq. (16)). These relationships are presented in Fig. 3 for only the K_x components. The K_y components are exactly the same since a square input aperture was assumed.

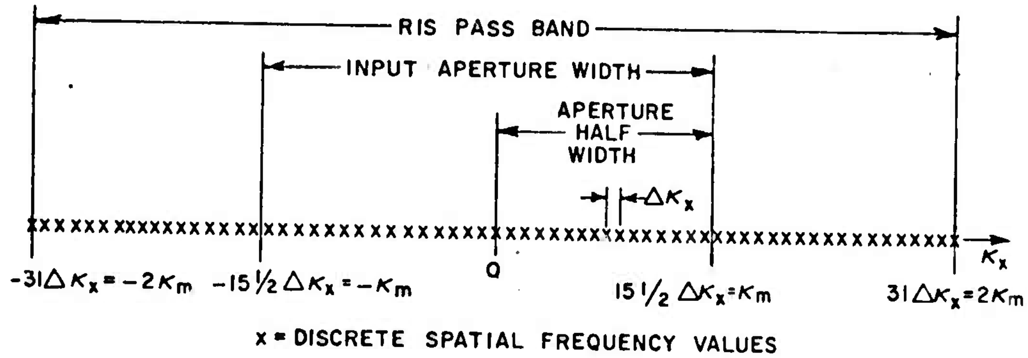

Fig. 3. Discrete frequency relationships.

The RIS passband is seen to be twice the input aperture width K_m which is the E-field pass band. This fact results from convolving the aperture function $W(K_x,K_y)$ with itself in Eq. (20).

E. Summary

At this point we have both a continuous mathematical model (Eq. (32)) and a discrete model (Eq. (35)) describing the restored image spectrum in terms of the parameters a_1, b_1, c_1, Δa_1, Δb_1, and Δc_1 which describe the turbulence-induced effects in the received E-field. The goal now is to use the discrete model, in conjunction with a high speed digital computer, to set limits on the ranges over which Δa_1, Δb_1, and Δc_1 may vary for a particular choice of a_1, b_1, and c_1 such that the restored image (i.e., inverse FFT of Eq. (35)) is a "good" approximation of the actual point object. The details of this "goodness" criterion are discussed in Chapter III, section E.

CHAPTER III
ANALYSIS OF THE RESTORED IMAGE SPECTRUM

A. Introduction

In this chapter we discuss in depth the concepts associated with restored images, their quality and the restored image spectrum (RIS) from which they are obtained. First, we define what we mean by an ideally restored image and the spectrum of this image. We then consider in detail how well the RIS, given in Eq. (32) of Chapter II, matches the ideal RIS. The major RIS degrading factors are found to be mathematical poles present in the RIS. Physically this theory is not difficult to accept since the poles represent gross departures from the ideally flat RIS. In order to facilitate a computer analysis of these poles, a series of equations are derived relating the number and location of these poles to the parameters describing the E-field phase expansion (Eq. (14)).

In order to measure the effectiveness of the restoration procedure described in Chapter I, it is necessary to describe a criterion with which to judge restored image quality. Therefore, we conclude this chapter with a discussion of three parameters chosen to describe the restored image quality.

B. Definition of the Ideally Restored Image

In this section the ideally restored image is defined for the degraded aperture plane E-field model presented in Chapter I. The mathematical expression for the ideally restored image is given for the continuous and discrete cases. And finally, a brief discussion of the non-ideally restored image is presented.

The ideally restored image is defined in terms of the equations expressing the turbulence degraded E-field wavefronts. These aperture plane E-field distributions for the object point and reference point are reproduced below in Eqs. (36a) and (36b), respectively:

$$\text{(36a)} \quad E_a(K_x,K_y) = e^{j(d_i/k)^2(aK_x{}^2+bK_xK_y+cK_y{}^2)}$$

$$\text{(36b)} \quad E_a(K_x,K_y) = e^{j(d_i/k)^2((a+\Delta a)K_x{}^2+(b+\Delta b)K_xK_y+(c+\Delta c)K_y{}^2)} .$$

For the special case in which $\Delta a = \Delta b = \Delta c = 0$, both Eqs. (36a) and (36b) have exactly the same mathematical form. This means that both waves were perturbed in exactly the same manner as they propagated through the turbulent atmosphere. Thus, using the MTF obtained from Eq. (36b) to restore the degraded image characterized by Eq. (36a), we define the ideally restored image as the image obtained when $\Delta a = \Delta b = \Delta c = 0$. This definition, an extension of Harris's [9] work, does not restrict the values of a, b, and c. Physically, this means that as long as both the reference wave and the object wave experience the same turbulence effects, as characterized by a, b, and c, the best possible restored image is obtained.

Applying the condition that $\Delta a = \Delta b = \Delta c = 0$ (equivalently $\Delta a_1 = \Delta b_1 = \Delta c_1 = 0$) to the continuous RIS in Eq. (32) and taking the inverse Fourier transform of this function, an expression is obtained for the ideally restored image.

$$(37a) \qquad I_R(x_1,y_1) = \frac{1}{(2\pi)^2}\iint_{-2K_m}^{2K_m} R(K_x,K_y,a_1,b_1,c_1,0,0,0)e^{j(K_xx_1+K_yy_1)}dK_xdK_y$$

$$(37b) \qquad = \frac{1}{(2\pi)^2}\iint_{-2K_m}^{2K_m} 1\; e^{j(K_xx_1+K_yy_1)}dK_x\, dK_y$$

$$(37c) \qquad = \left(\frac{2K_m}{\pi}\right)^2 \frac{\text{Sin}\; 2K_mx_1}{2K_mx_1}\;\frac{\text{Sin}\; 2K_my_1}{2K_my_1}$$

Note that the result obtained in Eq. (37c) is not the ideal point object, $\delta(x_1,y_1)$; however, in the limit as $K_m \to \infty$, Eq.(37c) does approach this ideal result, a fact well known from diffraction theory. Thus, the system band limit $2K_m$ has imposed an upper bound on the restored image quality even in the ideal case.

When the discrete case (Eq. (35)) is considered for $\Delta a = \Delta b = \Delta c = 0$ (equivalently $\Delta a_1 = \Delta b_1 = \Delta c_1 = 0$), we must recall that the FFT algorithm represents the function being transformed as a discrete Fourier series (see Appendix C). The results indicate that when $R(p\;\Delta K_x,\; q\;\Delta K_y,\; a_1,\; b_1,\; c_1,\; 0,\; 0,\; 0)$, which equals 1.0 at all discrete frequencies, is inverse Fourier transformed; the resulting function is the discrete analogy to the Dirac delta function. For this case, the discrete restored image is:

$$(38) \qquad I_R(p\;\Delta x_1,q\;\Delta x_1) = \delta(p\;\Delta x_1,q\;\Delta y_1)$$

where p and q are integers that specify the location of the restored image in the 6 x 64 sample restored image array.

Neither Eq. (37c) nor (38) is the ideal $\delta(x_1,y_1)$ point object but these functions do represent the best possible approximation of $\delta(x_1,y_1)$ for the band limited system we are considering. Thus, they will hereafter be referred to as the ideally restored images.

Next, consider the case for which Δa_1, Δb_1, and Δc_1 are permitted to assume small positive or negative values. For this case, the received E-field distributions for the reference point and object point will be different (see Eqs. (36a) and (36b)). Thus, since the PSF is no longer the impulse response of exactly the same linear imaging system that degrades the point object, we expect the restored image quality to fall short of the ideally restored image. This fact emphasizes the need for a analysis of the degrading effects of finite Δa_1, Δb_1 and Δc_1.

C. Analysis of the Restored Image Spectrum (RIS)

In section B it was suggested that when Δa, Δb and Δc (or equivalently Δa_1, Δb_1 and Δc_1) are finite, attempted image restoration would fall short of producing the ideally restored image. In this section, using the RIS, it will be shown that indeed this situation does occur. The loci of poles in the RIS are shown to be the determining factors in the restored image quality. A thorough mathematical analysis of the number and location of these pole loci is thus presented.

The restored image obtained when Δa_1, Δb_1 and Δc_1 are finite is demonstrated to be non-ideal by returning to the RIS given in Eq. (32). When $\Delta a_1 = \Delta b_1 = \Delta c_1 = 0$, $R(K_x,K_y,a_1,b_1,c_1,0,0,0)$ is equal to 1.0 for all frequencies within the system passband. This spectrum, when inverse transformed, yields the ideally restored image calculated in Eq. (37c). However, when Δa_1, Δb_1 and Δc_1 are finite, the RIS includes terms involving the Cot function. Obviously when a Cot $n\pi = \infty$ (n integer) condition occurs (i.e., a pole exists), the frequency component will greatly exceed the desired value of 1.0. The restored image which is the inverse Fourier transform of this degraded RIS will fail to be the ideally restored image.

The continuous form for the RIS is used in this section; however, it should be remembered that at any point in the analysis the discrete results may be obtained by making the substitutions given in Eqs. (34a) and (34b).

Returning to the RIS, which is reproduced below in Eq. (39), note that the poles are introduced whenever the Cot argument, which we define as the function $Z(K_x,K_y)$, assumes the value $Z = n\pi$ (n = integer).

$$(39)\qquad R(K_x,K_y,a_1,b_1,c_1,\Delta a_1,\Delta b_1,\Delta c_1) = \left[1 + \frac{2\Delta a_1 K_x + \Delta b_1 K_y}{2a_1 K_x + b_1 K_y}\right]$$

$$\left[1 - \left\{(2\pi/K_m^2)^{1/2}(2K_m-|K_x|)(2\Delta a_1 K_x+\Delta b_1 K_y)\right\}\mathrm{Cot}\left\{(2\pi/K_m^2)^{1/2}(2K_m-|K_x|)\right.\right.$$

$$\left.\left.\cdot(2(a_1+\Delta a_1)K_x + (b_1+\Delta b_1)K_y)\right\}\right]\left[1 + \frac{2\Delta c_1 K_y+\Delta b_1 K_x}{2c_1 K_y+b_1 K_x}\right]$$

$$\left[1 - \left\{(2\pi/K_m^2)^{1/2}(2K_m-|K_y|)(2\Delta c_1 K_y+\Delta b_1 K_x)\right\}\mathrm{Cot}\left\{(2\pi/K_m^2)^{1/2}(2K_m-|K_y|)\right.\right.$$

$$\left.\left.\cdot(2(c_1+\Delta c_1)K_y + (b_1+\Delta b_1)K_x)\right\}\right] \quad .$$

Since both square-bracketed terms involving the Cot function have the same mathematical form, we need only analyze one such term. The other term will follow with the proper substitution of wavefront parameters. Thus, we need only analyze the term involving the a and b parameters. The Cot argument, $Z(K_x,K_y)$, for this term is given in Eqs. (40a) and (40b) below.

$$(40a)\qquad Z(K_x,K_y) = (2\pi/K_m^2)^{1/2}(2K_m-|K_x|)(2a_pK_x + b_pK_y)$$

$$(40b)\qquad = (\pi/K_m^2)\left[-2a_pK_x|K_x|-b_p|K_x|K_y + 4a_pK_mK_x + 2b_pK_mK_y\right]$$

The parameters a_p, b_p and c_p are defined below as:

$$(41a)\qquad a_p = a_1 + \Delta a_1$$

$$(41b)\qquad b_p = b_1 + \Delta b_1$$

$$(41c)\qquad c_p = c_1 + \Delta c_1 \quad .$$

Eq. (40b) is an odd function of K_x and K_y; that is,

$$Z(K_x,K_y) = -Z(-K_x,-K_y).$$

Thus, the analysis may be further limited to the half plane defined by:

$$K_x \geq 0 \quad , \quad -2K_m \leq K_y \leq 2K_m \quad .$$

The analysis for the second half plane is obtained by substituting $-K_x$ for K_x and $-K_y$ for K_y into the equations derived below and then multiplying by -1.0.

As stated previously, the loci of poles are determined by the condition $Z(K_x,K_y) = n\pi$ (n integer). The maximum number of such pole loci is obviously proportional to the maximum range of $Z(K_x,K_y)$. Knowledge of this range, in terms of a_p and b_p, affords control over the number of pole loci. This facilitates a computer analysis of the effects of these parameters on the restored image quality.

In order to determine this maximum range, we must first generate an equation in terms of a_p and b_p and determine the maximum and minimum values assumed by $Z(K_x,K_y)$. We will find that this analysis is divided into two cases depending on the relative magnitudes of a_p and b_p.

Using the first and second derivatives of Z with respect to K_y to determine maxima or minima with respect to K_y, we find that:

(42a) $$\frac{\partial Z}{\partial K_y} = 0 \qquad \Rightarrow \qquad K_x = 2K_m$$

and

(42b) $$\frac{\partial^2 Z}{\partial K_y^2} = 0 \quad .$$

Substituting Eq. (42a) into Eq. (40b) we find that $Z(K_x,K_y) \equiv 0$ for all K_y. Since Eq. (42b), the second derivative test for maxima or minima fails, we deduce that there are no maxima or minima along the line $K_x = 2K_m$.

From the first and second derivatives of Z with respect to K_x we find, with respect to K_x, that:

(43a) $$\frac{\partial Z}{\partial K_x} = 0 \qquad \Rightarrow \qquad K_y = \frac{4a_p}{b_p}(K_m-K_x)$$

and

(43b) $$\frac{\partial^2 Z}{\partial K_x^2} = -\frac{4a_p}{b_p} \quad .$$

Here, the second derivative test indicates that maxima do exist, for $a_p/b_p > 0$ (or minima for $a_p/b_p < 0$), along the line $K_y=(4a_p/b_p)(K_m-K_x)$. This equation is graphed in Fig. 4.

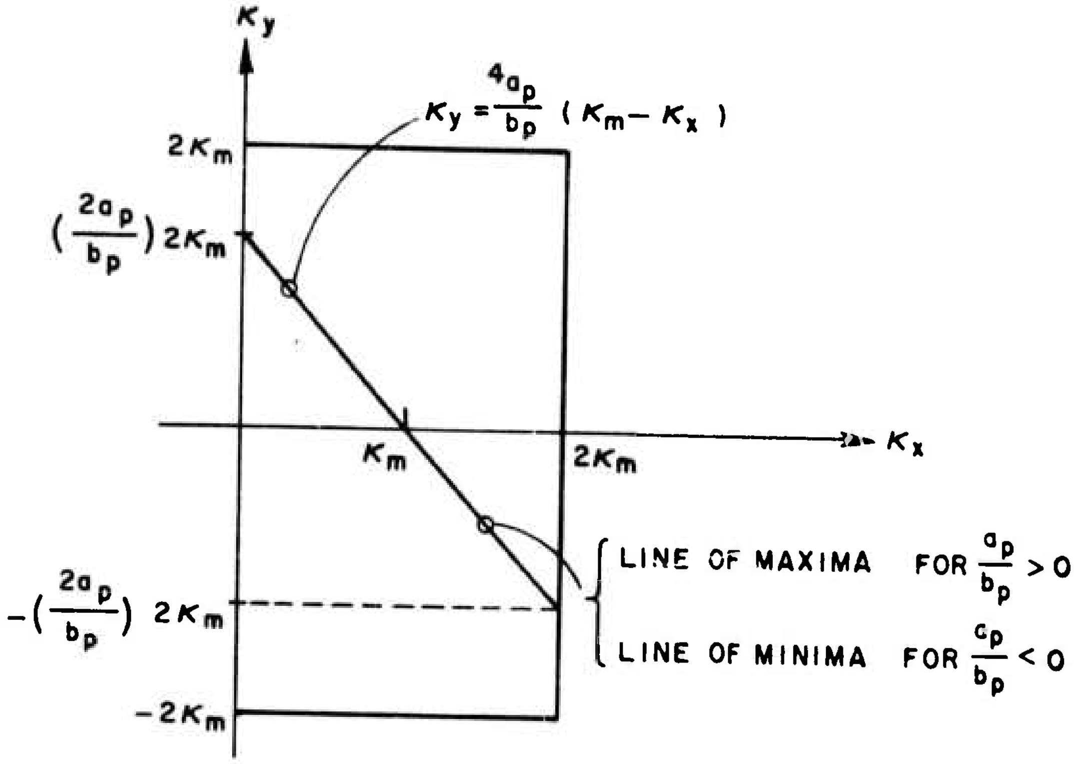

Fig. 4. Maxima and minima of $Z(K_x,K_y)$.

Evaluating Eq. (40b) along the line $K_y = (4a_p/b_p)(K_m-K_x)$, we have:

$$(44) \qquad Z\left(K_x, K_y = \frac{4a_p}{b_p}(K_m-K_x)\right) = (\pi/K_m^2)(2a_pK_x^2 - 8a_pK_mK_x + 8a_pK_m^2) \quad ,$$

which is graphed in Fig. 5. Fig. 5 indicates that the maxima, with respect to K_x exist at $K_x = 0$ and $K_y = (2a_p/b_p)2K_m$ (also, see Fig. 4).

Now, looking at the Z versus K_y variation with $K_x = 0$, we find from Eq. (40b) that:

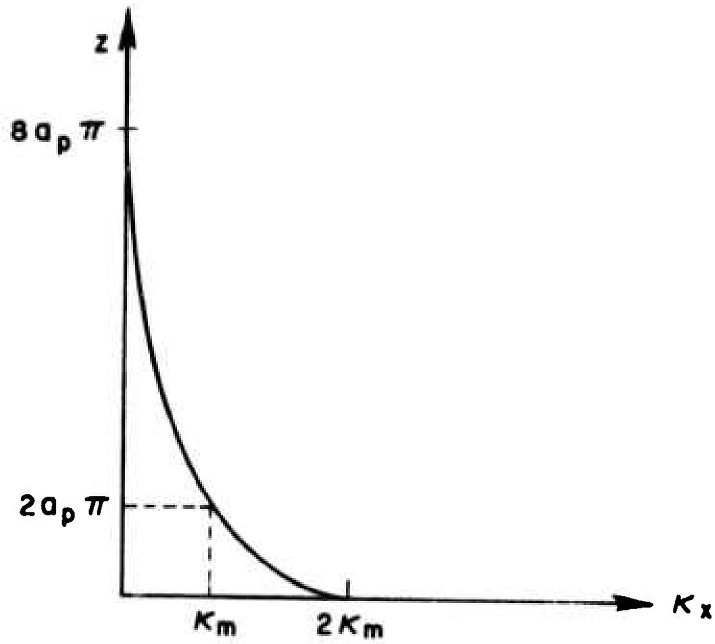

Fig. 5. Z evaluated along line of maxima or minima vs. K_x.

(45) $$Z(0,K_y) = (\pi/K_m^2)\, 2b_pK_mK_y \quad ,$$

which has a maximum at $K_y = 2K_m$ as seen in Fig. 6. Thus, when $b_p \geq 2a_p$, the maximum value of Z occurs at $(0,2K_m)$. Since Z has been shown to be an odd function of K_y, the minimum must occur at the point $(0,-2K_m)$ as shown in Fig. 6. Thus, the maximum range of Z, the quantity we are interested in, for $b_p \geq 2a_p$ is:

(46) $$Z_{max} - Z_{min} = 4b_p\pi - (-4b_p\pi) = 8b_p\pi \quad .$$

The parameter b_p in Eq. (46) determines the maximum number of pole loci contributed to the restored image spectrum.

When $b_p < 2a_p$, a different situation exists. The results obtained from Eq. (43a) and Fig. 4 indicate that the maximum value of Z with respect to K_x occurs at the intersection of the lines $K_y = 2K_m$ and

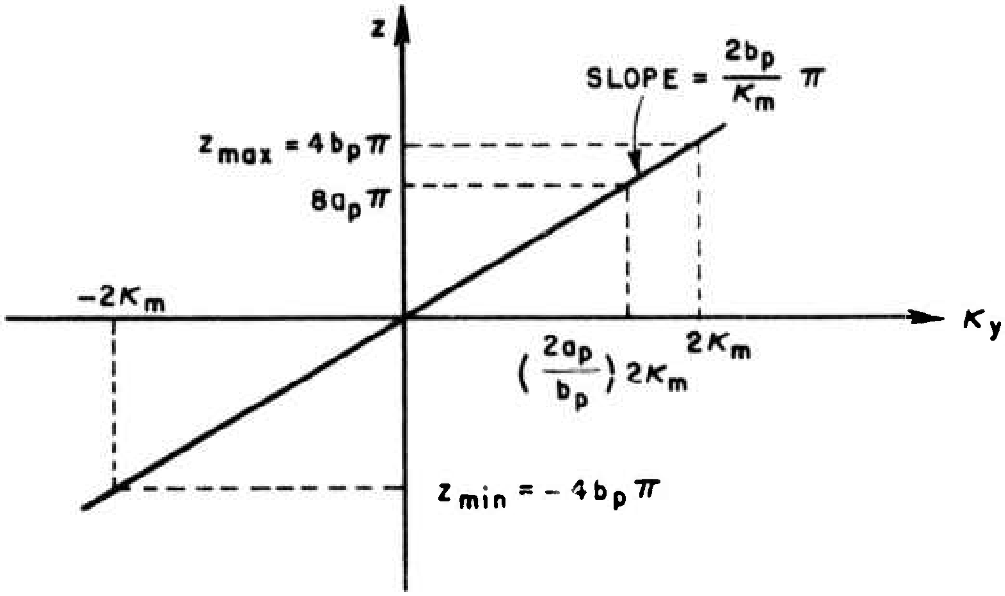

Fig. 6. Z_{max} and Z_{min} as a function of K_y.

$K_y = (4a_p/b_p)(K_m-K_x)$ or, by substituting $K_y = 2K_m$ into $K_y = (4a_p/b_p)$ (K_m-K_x), at the point:

(47a) $\quad K_x = K_m(1 - \frac{b_p}{2a_p})$

(47b) $\quad K_y = 2K_m$.

This result, which is valid for $-2a_p \leq b_p \leq 2a_b$, is shown in Fig. 7.

Consider a (K_y,Z) plane cutting through Fig. 7 along the line $K_x = K_{x_0}$. By substituting $K_x = K_{x_0}$ into Eq. (40b) and regrouping terms, we obtain:

(48) $\quad Z(K_{x_0},K_y) = (\pi/K_m^2)\left[(2b_pK_m-b_pK_{x_0})K_y+4a_pK_mK_{x_0}-2a_pK_{x_0}^2\right]$,

which is graphed in Fig. 8.

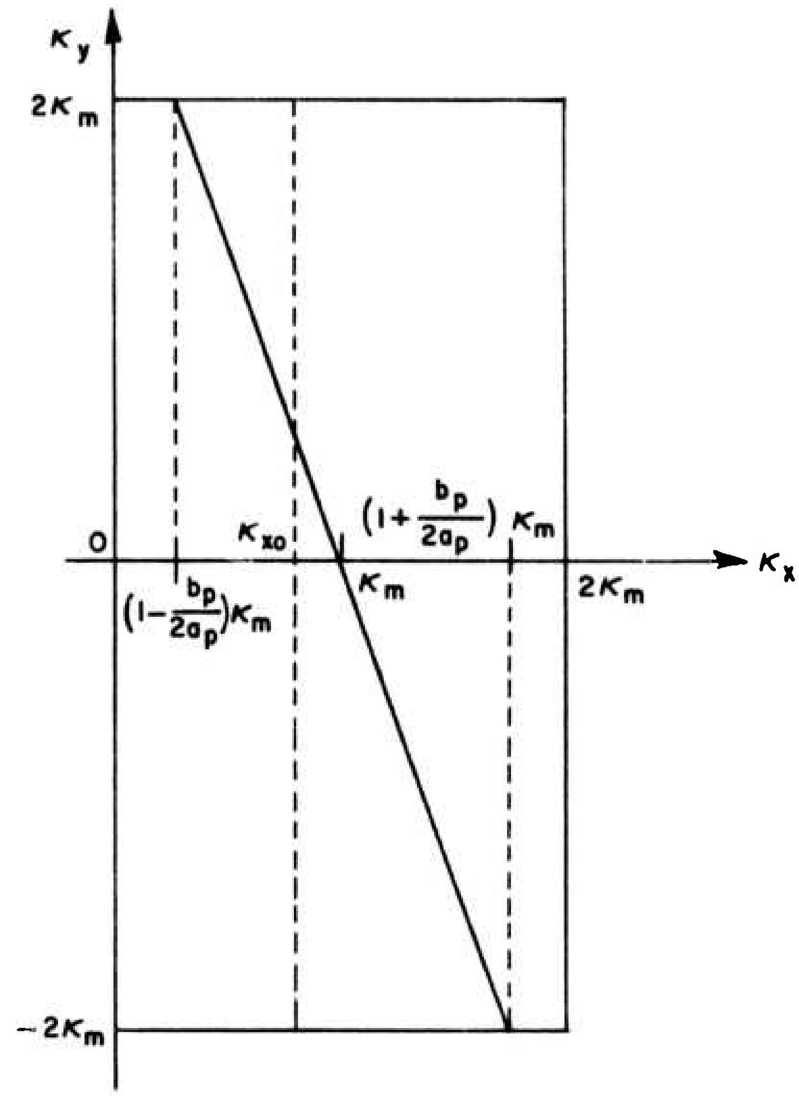

Fig. 7. Location of Z_{max} for $-2a_p < b_p \leq 2a_p$.

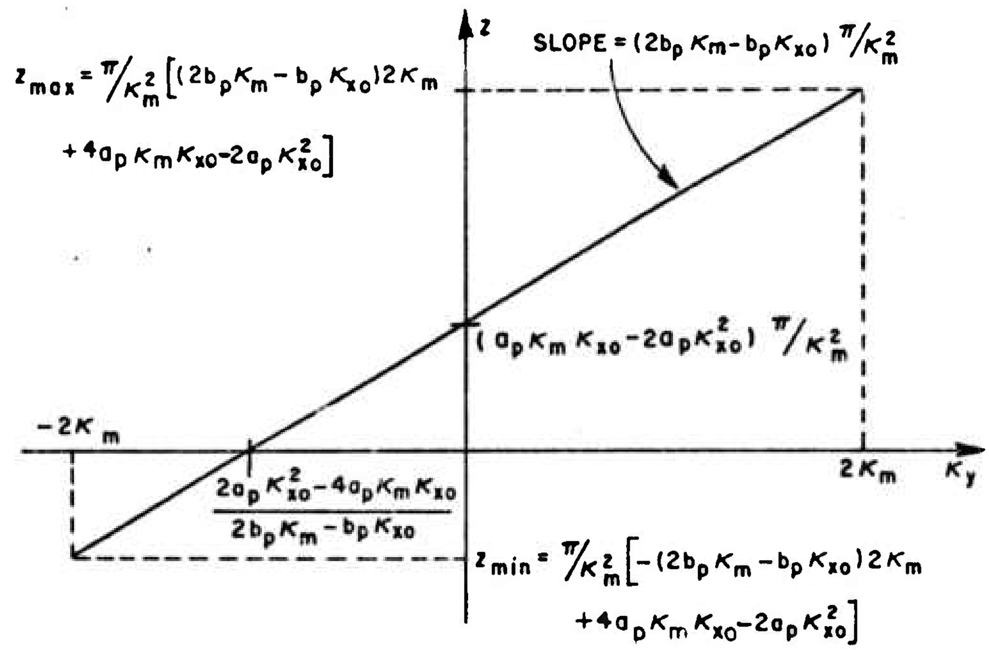

Fig. 8. Z_{max} and Z_{min} as a function of K_y.

In Fig. 8 it is seen that the maximum value of Z, with respect to K_y, occurs along the line $K_y = 2K_m$. In Fig. 7, it was demonstrated that, for $-2a_p \leq b_p \leq 2a_p$, the maximum value of Z with respect to K_x occurs along the line $K_x = K_m(1 - (b_p/2a_p))$. Evaluating Z_{max} (from Fig. 8) at the point $(K_x = K_m(1-(b_p/2a_p)), K_y = 2K_m)$, we find:

$$Z_{max} = \left[2a_p + 2b_p + \frac{b_p{}^2}{2a_p}\right]\pi \qquad (49)$$

Since the Z axis intercept in Fig. 8 will always be greater than or equal to zero for $0 \leq K_x \leq 2K_m$, the minimum value of Z will always occur (see Fig. 6) at the point $(K_x = 0, K_y = -2K_m)$, thus:

$$(50) \qquad Z_{min} = -4b_p\pi \quad .$$

Using Eqs. (49) and (50), the maximum range for Z, when $-2a_p \leq b_p \leq 2a_p$, is calculated to be:

$$(51) \qquad Z_{max} - Z_{min} = (2a_p + 6b_p + \frac{b_p^2}{2a_p})\,\pi \quad .$$

In this case the magnitudes of both the parameters a_p and b_p contribute to the total number of pole loci present in the RIS. Dividing the maximum ranges for Z found in Eqs. (46) and (51) by π, and then substituting

$$a_p = a_1 + \Delta a_1$$

$$b_p = b_1 + \Delta b_1 \quad ,$$

we find that the maximum number of pole loci M_p (M_p integer) is:

$$(52a) \qquad \text{for} \quad 2(a_1 + \Delta a_1) \leq b_1 + \Delta b_1 \quad ,$$

$$(52b) \qquad M_p = 8|b_1 + \Delta b_1|$$

and for

$$(53a) \qquad -2(a_1 + \Delta a_1) \leq b_1 + \Delta b_1 \leq 2(a_1 + \Delta a_1) \quad ,$$

$$(53b) \qquad M_p = \left|2(a_1 + \Delta a_1) + 6(b_1 + \Delta b_1) + \frac{(b_1 + \Delta b_1)^2}{2(a_1 + \Delta a_1)}\right| \quad .$$

The gross characteristics of the pole loci in the RIS are determined in Eqs.(52b) and (53b) by the parameters a_1 and b_1, which are a measure of the wavefront distortion at the edge of the input aperture in fractions of a wavelength; however, the perturbation parameters Δa_1 and Δb_1 contribute in two important ways. First, they may increase or decrease the value of M_p by a sufficient magnitude to actually introduce or remove a loci of poles. Second, regardless of whether they do introduce or remove a loci of poles, the perturbation parameters will always tend to shift the location of the existing loci of the poles in the K_xK_y plane. This second point is important in terms of the discrete case in which a small change in Δa_1 or Δb_1 may result in a discrete frequency component being evaluated precisely at a pole. The implications of this event are covered in Chapter IV, section B.

One additional point should be covered before completing this analysis of the RIS. This point involves the term

$$\Delta Z = \pi/K_m{}^2[-2\Delta a_1 K_x|K_x|-\Delta b_1|K_x|K_y+4\Delta a_1 K_m K_x+2\Delta b_1 K_m K_y] \tag{54}$$

which multiplies the Cot function in Eq. (39). It was stated previously in Chapter II, section C, that the ranges for Δa_1 and Δb_1 are much less than 1.0. Thus, since ΔZ and $(\partial\Delta Z/\partial K_x)$ and $(\partial\Delta Z/\partial K_y)$ are all proportional to these perturbation parameters, this implies that the function Z is small and slowly varying in both the K_x and K_y directions. This multiplicative term then tends to modulate the Cot function in such a way as to reduce the area under the Cot function. In the next chapter this will be demonstrated to be particularly important near RIS poles.

The most significant results obtained from the RIS analysis are given in Eqs. (52b) and (53b). These equations are emphasized because they relate the maximum number of RIS pole loci, which have been hypothesized to have a significant bearing on the restored image quality, to the parameters used to describe the turbulence degraded input waves (see Eqs. (36a) and (36b)). These relationships will be used in Chapter IV, section B, where actual image restoration is performed on three classes of degraded images.

D. The Defocused Image Case

At this point, a particular class of degraded images is selected for analysis. This class of images is distinguished by the absence of the coupling between K_x and K_y in Eqs. (36a) and (36b). That is, we set the parameters $b = \Delta b = 0$ (or equivalently $b_1 = \Delta b_1 = 0$) in all equations involving the wavefront parameters. A review of these equations is contained in this section.

Physically, this case (i.e., $b_1 = \Delta b_1 = 0$) corresponds to the recording of defocused images in the telescope image plane. This case is very useful when one is studying the relationship between poles in the RIS and the quality of the resulting restored image. It is useful because the associated mathematics are simpler than those for the case involving the cross term $b_1 + \Delta b_1$ but yet loci of poles are present in the RIS and they do tend to degrade the restored image quality.

In the following discussion, the general equations derived in Chapters II and III are restated with the cross-coupling terms b and Δb (or equivalently b_1 and Δb_1) set equal to zero.

The aperture plane E-field distribution taken from Eq. (36a) is rewritten for this special case in Eq. (55) below.

$$(55) \qquad E_a(K_x,K_y) = e^{j(d_i/k)^2(aK_x^2 + bK_y^2)}$$

Assuming this phase distribution, the degraded image spectrum (aperture plane correlation function, $C(K_x,K_y)$, and the MTF, $H(K_x,K_y)$, have the following forms (the general equations are (24) and (28)).

$$(56) \qquad C(K_x,K_y) = \left[(2K_m-|K_x|)\frac{\sin(d_i/k)^2(2K_m-|K_x|)aK_x}{(d_i/k)^2(2K_m-|K_x|)aK_x}\right] \cdot$$

$$\left[(2K_m-|K_y|)\frac{\sin(d_i/k)^2(2K_m-|K_y|)cK_y}{(d_i/k)^2(2K_m-|K_y|)cK_y}\right]$$

$$(57) \qquad H(K_x,K_y) = \left[(2K_m-|K_x|)\frac{\sin(d_i/k)^2(2K_m-|K_x|)(a+\Delta a)K_x}{(d_i/k)^2(2K_m-|K_x|)(a+\Delta a)K_x}\right] \cdot$$

$$\left[(2K_m-|K_y|)\frac{\sin(d_i/k)^2(2K_m-|K_y|)(c+\Delta c)K_y}{(d_i/k)^2(2K_m-|K_y|)(c+\Delta c)K_y}\right]$$

Note that Eqs. (56) and (57) are separable into two factors, one involving only K_x and the other involving only K_y. Thus the behavior of each factor is graphed in a single figure (Fig. 9), where K represents either K_x or K_y and γ represents a or c. The total function is then obtained by multiplying two such diagrams together at each point in the K_xK_y plane.

The restored image spectrum (RIS) for the special case becomes (from Eq. (32)):

$$(58) \qquad R(K_x,K_y,a_1,0,c_1,\Delta a_1,0,\Delta c_1) = \frac{C(K_x,K_y)}{H(K_x,K_y)} =$$

$$\left[\left(1+\frac{\Delta a_1}{a_p}\right)\left(1-\left\{\frac{2\pi}{K_m^2}(2K_m-|K_x|)\Delta a_1K_x\right\}\mathrm{Cot}\left\{(2\pi/K_m^2)(2K_m-|K_x|)a_pK_x\right\}\right)\right] \cdot$$

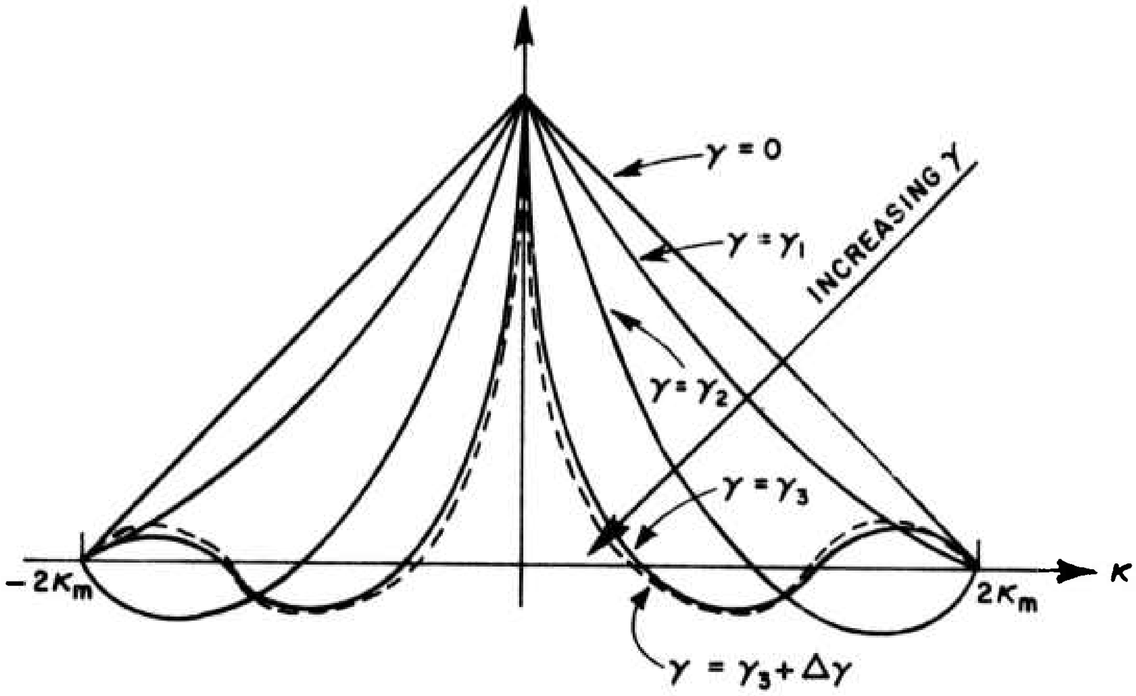

Fig. 9. Graph of $(2K_m-|K|)$ Sinc$[(di/k)^2\ (2K_m-|K|)\gamma K]$.

$$\left[\left(1+\frac{\Delta c_1}{c_p}\right)\left(1-\left\{(2\pi/K_m^2)(2K_m-|K_y|)\Delta c_1 K_y\right\}\text{Cot}\left\{(2\pi/K_m^2)(2K_m-|K_y|)c_p K_y\right\}\right)\right]$$

Note that each factor in Eq. (58) involves only K_x or K_y; thus, the overall inverse transform is the product of two one-dimensional inverse transforms.

The discrete form of Eq. (58) is obtained by substituting Eqs.(34a) and (34b) into Eq. (58) to yield:

(59) $\quad R(p\ \Delta K_x,\ q\ \Delta K_y,\ a_1,\ 0,\ c_1,\ \Delta a_1,\ 0,\ \Delta c_1)\quad .$

The number of pole loci for this special case is obtained from Eqs. (52b) and (53b). Obviously $b_p = 0$ satisfies Eq. (53a); thus the number of pole loci is

(60a) $$M_{px} = 2(a_1 + \Delta a_1) = 2|a_p| .$$

Eq. (60a) indicates that the K_x term in Eq. (58) contributes $2a_p$ loci of poles in each half plane (i.e., $K_x < 0$ and $K_x > 0$). Similar results are obtained for the K_y term in Eq. (58), where the two K_y half planes (i.e., $K_y \leq 0$ and $K_y \geq 0$) each contribute

(60b) $$M_{py} = 2(c_1 + \Delta c_1) = 2|c_p|$$

loci of poles. The number of pole loci equals minimum integer value of Eqs. (60a) and (60b).

The actual loci of poles are demonstrated to be straight lines by solving the equation:

(61) $$Z(K_x, K_y) = n\pi$$

where $Z(K_x, K_y)$ is the Cot argument from Eq. (58) and n is an integer. As an example of this calculation, consider the K_x half plane defined by $0 \leq K_x \leq 2K_m$ and $-2K_m \leq K_y \leq 2K_m$. Solving Eq. (61) for these conditions we obtain

(62a) $$Z(K_x, K_y) = -\frac{2\pi a_p}{K_m^2} K_x^2 + \frac{4\pi a_p}{K_m} K_x = n\pi$$

which reduces to

(62b) $$K_x = K_m \pm K_m \sqrt{\frac{2a_p - n}{2a_p}} .$$

Eq. (62b) is indeed the equation for two straight lines located equal distances on either side of the line $K_x = K_m$. The loci in the remaining K_x half plane and the two K_y half planes follow from similar calculations. An overall view of these pole loci is presented in Fig. 10. The Z versus K_x and Z versus K_y graphs clearly illustrate that the pole loci arise when the Cot argument $Z = n\pi$ ($n = 1$ for Fig. 10).

Note that when a_p is incremented by a small amount to a new larger value a_p', the loci of poles shift in the RIS.

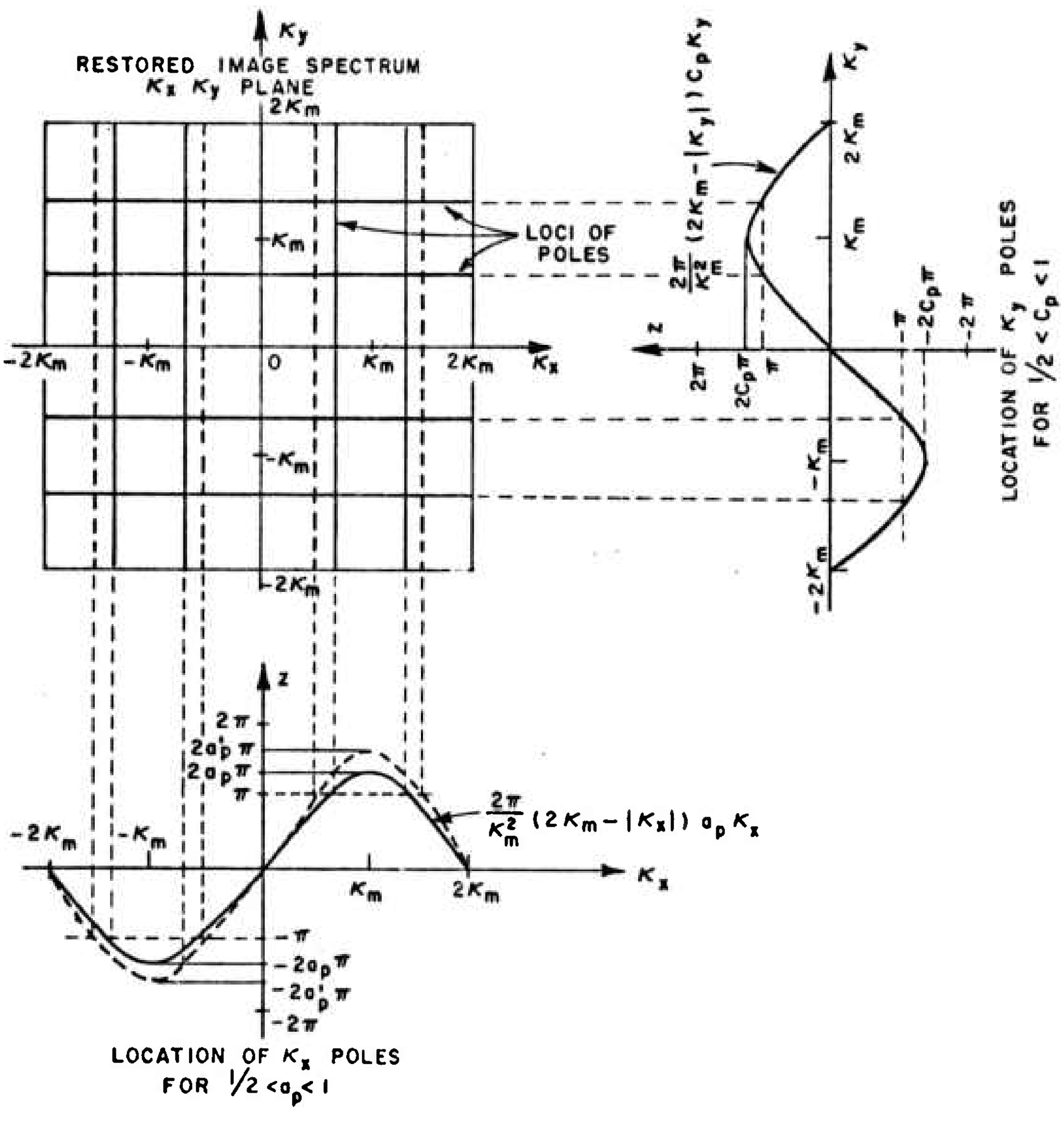

Fig. 10. Location of pole loci in the RIS.

At this point, all the significant equations from Chapter II and Chapter IIIA, B and C have been rewritten for the special case in which there is no cross coupling between K_x and K_y (i.e., $b_1 = \Delta b_1 = 0$). Note that Fig. 10, which illustrates the location and shifting of pole loci, is a very important graph and it is referred to several times in Chapter IV where actual image restoration of degraded images having zero cross coupling between K_x and K_y (i.e., defocused image case) is discussed.

E. Restored Image Quality Criterion

This section is devoted to a discussion of the criterion by which the restored quality is judged. Among the authors who have addressed themselves to this problem have been Linfoot [16] and Barry [17]. They have emphasized that it is desirable for such a criterion to reflect a quantitative rather than subjective measure of the restored image quality. For this reason, three parameters, the restored Strehl ratio (Sr), the restored image integral scale (r) and the restored image mean squared error (ϵ_{ms}), were selected to describe the restored image quality. A discussion of each of these parameters and their optimum values comprises the material discussed in this section.

The Strehl ratio is defined as:

$$(63)\qquad S = \frac{I_i(0,0)}{I_I(0,0)}$$

where $I_i(0,0)$ is the point spread function (PSF) of the turbulence degraded imaging system and $I_I(0,0)$ is the PSF for the ideal turbulence free system. However, for this study in which we are interested in restored image quality, we define a restored Strehl ratio as:

$$(64)\qquad Sr = \frac{I_R(0,0)}{I_I(0,0)}$$

where $I_R(0,0)$ is the restored image obtained from the RIS and $I_I(0,0)$ is the ideally restored image. For the optimum case (with a point source input) the ideally restored image has the value $I_I(0,0) = 1.0$. Substituting this condition into Eq. (64), we see that the restored Strehl ratio (Sr) is merely the restored image value at the coordinate system origin. Thus, for the ideally restored image (see Eq. (38)), $Sr = I_R(0,0) = 1.0$.

The restored Strehl ratio yields both spatial domain (x_1,y_1) and spatial frequency (K_x,K_y) information about the restored image. In terms of the spatial domain, Sr is the ratio of the central intensity peaks of the restored image and the ideal image. For the spatial frequency interpretation, we recall that, in terms of Fourier transforms, $I_R(0,0)$ and $I_I(0,0)$ may be written as:

$$\text{(65a)} \qquad I_R(0,0) = (1/2\pi)^2 \iint_{-2K_m}^{2K_m} R \, dK_x \, dK_y$$

and

$$\text{(65b)} \qquad I_I(0,0) = (1/2\pi)^2 \iint_{-2K_m}^{2K_m} 1.0 \, dK_x \, dK_y \quad .$$

Eqs. (65a) and (65b) are the average value of their respective spatial frequency spectrum. This means that the restored Strehl ratio may also be thought of as the RIS average value since the average value of the ideally restored image spectrum is 1.0 (all frequency components in the spectrum of the ideally restored image are equal to 1.0). Thus, the restored Strehl ratio, which has the optimum value of 1.0, gives us a measure of how closely the restored image and the RIS approach their ideal values.

The integral scale r_o is defined as:

$$\text{(66)} \qquad r_o = + \sqrt{\frac{\sum_{p=1}^{63} \sum_{q=1}^{63} I_R(p \, \Delta x, q \, \Delta y)}{\pi \; I_R(0,0)}}$$

where r_o is defined such that the volume of a cylinder with height $I_R(0,0)$ (restored image value at the origin) and radius r_o equals the volume under the restored image intensity function $I_R(x_1,y_1)$. This definition is illustrated in Fig. 11. The parameter r_o gives a measure of the spread of the restored image. The optimum value of r_o is $r_o = 1/\sqrt{\pi}$ which occurs when the integral in Eq. (66) equals $I_R(0,0)$.

If Eq. (65) is divided by $1/\sqrt{\pi}$, a normalized integral scale is defined as

$$\text{(67)} \qquad r = \sqrt{\pi} \, r_o \ ,$$

for which the optimum value of r is r = 1.0. It is the normalized integral scale that will be used in this study to express the spread of the restored image.

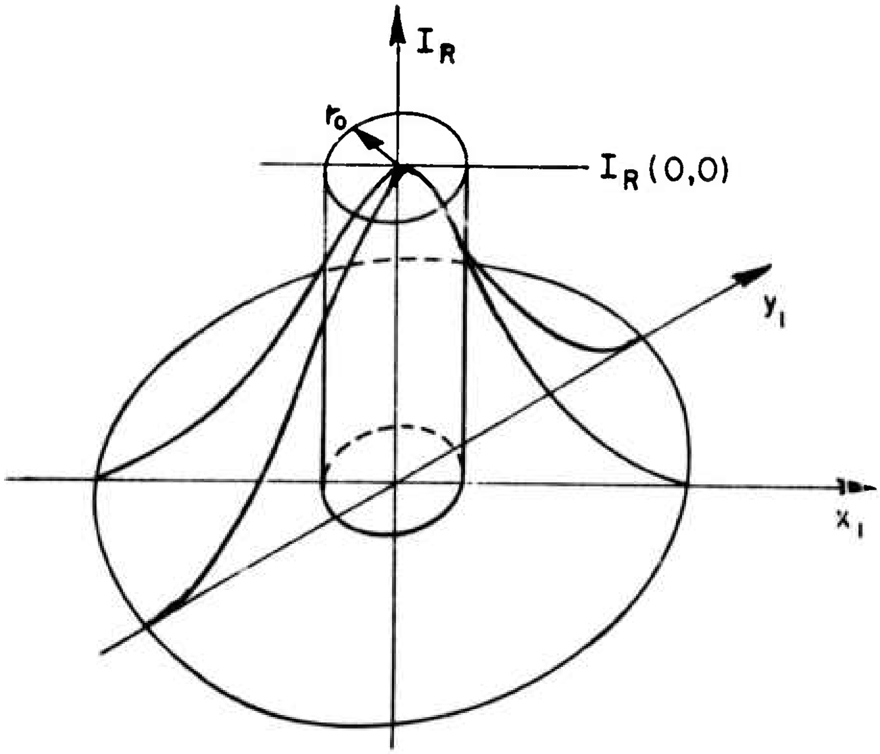

Fig. 11. Diagram illustrating the definition of r_o the integral scale.

The final restored image quality parameter is the restored image mean squared error (ε_{ms}). This parameter is defined as:

$$\varepsilon_{ms} = \left(\frac{1}{64}\right)^2 \sum_{p=0}^{63} \sum_{q=0}^{63} \left\{ I_R(p\ \Delta x,\ q\ \Delta y) - I_I(p\ \Delta x,\ q\ \Delta y) \right\}^2 \qquad (63)$$

where I_R and I_I are the restored and ideal images, respectively.

The parameter ε_{ms} gives a measure of the mean squared error between the actual restored image and the ideally restored image. Obviously the optimum value for ε_{ms} is zero.

Next in the discussion of the restoration parameters is the application of the computer processing techniques to the ideally restored images defined by $\Delta a_1 = \Delta c_1 = 0$ and finite a_1 and c_1 (see Chapter III-B). The resulting restoration parameters calculated using Eqs. (64), (67) and (68) are defined as bench marks against which the parameters calculated for images having finite valued Δa_1 and Δc_1 may be compared.

After numerous computer runs using various values of a_1 and c_1 ($\Delta a_1 = \Delta c_1 = 0$), it was verified that the bench-mark values are independent of the values selected for a_1 and c_1.

Table 1 lists both the theoretical and the actual computer calculated values for each parameter.

TABLE 1

Parameter	Theoretical Value	Calculated Value ($\Delta a_1 = \Delta c_1 = 0$)
Sr	1.000	1.000
r	1.000	1.000
ε_{ms}	0.000	8.553×10^{-10}

The discrepancies between the theoretical and calculated values of ε_{ms} represent inherent computer processing errors; however, these errors are sufficiently small to be insignificant. Thus, the calculated values are accepted as the bench-mark parameters.

The ranges for Sr, r, and ε_{ms} which define a successfully restored image must be specified. A successfully restored image will be defined in this study as an image with the following properties:

(69a) $0.5 < Sr \leq 2.0$

(69b) $0.5 \leq r < 2.0$

(69c) $\varepsilon_{ms} < 0.1$.

The range for Sr allows a ±3 db deviation in the restored image central peak intensity. The spread of the restored image, as expressed by r, may vary by a ratio of 2:1 while the mean squared error must be less than 10%. These values for the quality parameters were selected on the basis of preliminary computer processed images. Obviously either more stringent or more relaxed requirements could have been imposed; however, this particular choice serves as a reasonable starting point for defining a successfully restored image.

This completes the discussion of the restored image quality criterion. The quality parameters, restored Strehl ratio (Sr), integral scale (r), and mean squared error (ϵ_{ms}), were defined and the limits within which successful image restoration occurs were specified for these parameters.

F. Summary

This chapter has been primarily devoted to the discussion of restored image spectrum (RIS) and the restriction of this general analysis for the defocused case in which there is no cross coupling between the K_x and K_y variables. The most significant result of this analysis is a series of equations (Eqs. (52b), (53b), (60a) and (60b)) relating the number of pole loci in the RIS to the wavefront parameters a_p, b_p and c_p.

A discussion of the ideally restored image and the restored image quality criterion, which determines whether a processed image may be classed as a successfully restored image, were also discussed in this chapter.

CHAPTER IV
RESULTS

A. Introduction

In this chapter, three classes of turbulence degraded images are restored using a computer processing technique which involves the Fourier transform method of image restoration. (This method was discussed in Chapter I.) Each class of degraded images is defined by the number and location of the pole loci present in the RIS. The success or failure of the attempted restorations is then discussed in terms of the restored image quality criterion (see Chapter III, section E). Graphs which present the behavior of the restored image quality parameter as a function of the wavefront perturbation parameters Δa_1 and Δc_1 are included. The allowable ranges for Δa_1 and Δc_1 over which successful image restoration does occur are defined with reference to these graphs. These limits on Δa_1 and Δc_1 are the primary goal of this study and they will be used to define the ranges of successful image restoration.

B. Restoration Results

It has been suggested in Chapter III, section C, that the presence of poles in the restored image spectrum (RIS), as determined by the parameters $a_p(=a_1 + \Delta a_1)$ and $c_p(=c_1 + \Delta c_1)$, is intimately related to the success or failure of the image restoration process. The remainder of this section is devoted to demonstrating the importance of these pole loci and their effects on the restored image quality. In this chapter, a series of computer processed restored images is generated in order to determine whether the presence of poles does indeed influence the allowable ranges for the parameters Δa_1 and Δc_1. Each restored image is obtained by calculating the discrete RIS (Eq. (59)) and then applying the inverse FFT algorithm to this function.

Because only those cases where $a_1 = c_1$ and $\Delta a_1 = \Delta c_1$ are being considered, all the results derived throughout the remainder of this chapter for a_1 and Δa_1 apply identically for c_1 and Δc_1.

The series of computer processed images was divided into three unique cases. For each case, the value of the parameter a_1, which describes the gross wavefront distortion at the edge of the input aperture, was specified so as to introduce the loci of poles at a known location in the RIS (see Fig. 10). For each selected value of a_1, a restored image was calculated for perturbations $\Delta a_1 = n(0.006\lambda)$ (where $n + \pm 0,1,2,\cdots 41$). The special situation in which $\Delta a_1 = 0.0$ corresponds to that of the ideally restored image. It occurs only when the degraded image and the PSF have experienced exactly the same turbulence effects characterized by the particular choice of a_1. The argument Z, which is taken from Eq. (58), is graphed for the three cases in which

$a_1 = 0.25\lambda$, 0.5λ or 0.75λ (equivalently, in terms of the polynomial coefficients introduced in Eq. (8b) these three cases are given by

$$a_4' = \frac{2\pi}{C_w X_m^2}(0.25\lambda), \quad \frac{2\pi}{C_w X_m^2}(0.50\lambda) \quad \text{or} \quad \frac{2\pi}{C_w X_m^2}(0.75\lambda)$$

while $a_5' = a_6' = 0$) in Fig. 12. This graph, which is similar to those used in Fig. 10, presents the locations of the pole loci in the RIS. The x's and o's along the K_x axis represent the initial locations (when $\Delta a_1 = 0.0$) of RIS pole loci for Cases II and III, respectively. These initial pole locations are defined by the intersections of the Cot argument with the lines $Z = n\pi$.

Each case has a unique characteristic over the processing range that extends from

(70) $\quad (a_1 - 0.246) \leq a_p \leq (a_1 + 0.246)$.

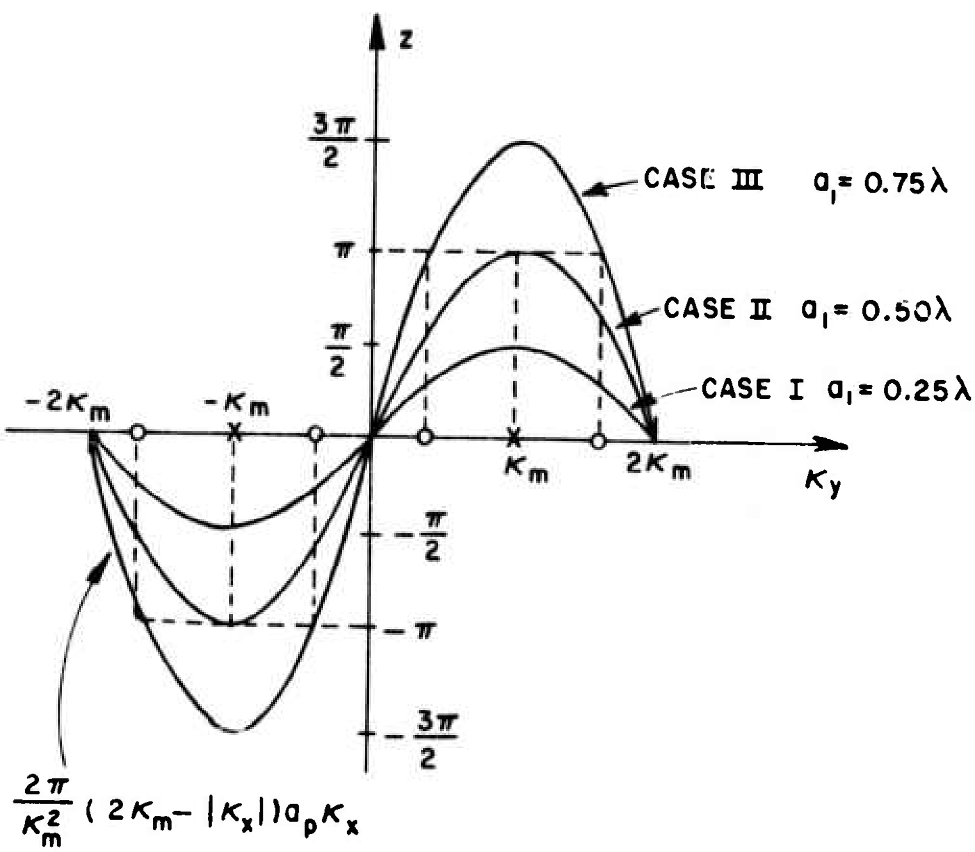

Fig. 12. Location of the points at which Cot argument $Z = n\pi$.

Case I is unique in that there are no pole loci introduced into the RIS over the processing range of a_p. Case II is unique in that when $a_p > a_1$ ($a_1 = 0.50\lambda$), a pair of pole loci is introduced at the point $|K_x| = K_m$ which then migrates away from this point as a_p increases. However, when $a_p < a_1$, this pair of pole loci is not present. Case III is unique in that a pair of pole loci is present for the entire processing range of a_p. This pair of pole loci migrates toward the point $|K_x| = K_m$ for $a_p < a_1$ and away from this point for $a_p > a_1$.

Figs. 13a, 13b, 13c, 14a, 14b, 14c, and 15a, 15b, 15c are graphs of the restored image quality factors: restored Strehl ratio (Sr), integral scale (r), and mean squared error (ε_{ms}) calculated from Cases I, II and III, respectively. Each quality factor is graphed as a function of Δa_1, the perturbation parameter. Note that on each graph, when $\Delta a_1 = 0.0$ ($a_p = a_1$), Sr = 1.0, r = 1.0 and ε_{ms} is a minimum. These are the expected results for the ideally restored image and occur on all graphs independent of the choice for a_1.

Examining Figs. 13a, 13b, and 13c, we see that for Case I ($a_1 = 0.25\lambda$) the range of Δa_1 over which successful image restoration occurs is limited at the value $\Delta a_1 = 0.11\lambda$ where the quality factor Sr exceeds the allowable upper bound of Sr = 2.0. Although Sr is the limiting parameter in this case, note that the two remaining quality parameters r and ε_{ms} are monotonically approaching their respective bounds at the point $\Delta a_1 = 0.11\lambda$. This behavior of r and ε_{ms} reinforces the assumption that, in the remaining portion of the region $\Delta a_1 > 0.11\lambda$, a successfully restored image cannot be obtained. Thus, the limits on Δa_1 for Case I are:

$$(71) \qquad -0.246\lambda \leq \Delta a_1 \leq 0.11\lambda$$

where -0.246λ is the lower processing limit for Δa_1 (see Eq. (70)).

Examination of Figs. 14a, 14b and 14c reveals that for Case II ($a_1 = 0.50\lambda$), when $\Delta a_1 > 0$, all three restoration parameters Sr, r, and ε_{ms} vary erratically. Hidden within these fluctuations we find regions in which the restoration parameters do indeed lie within the bounds that define a successfully restored image. However, there are adjacent regions in which the quality factors greatly exceed the allowable bounds, indicating that image restoration fails for these values of Δa_1.

Fig. 12 correlated with Figs. 14a, 14b and 14c indicates that this erratic behavior corresponds exactly with the introduction into the RIS of the first pair of pole loci. (This fact supports the hypothesis that the presence of poles in the RIS is directly related to restored image quality.) Furthermore, when $\Delta a_1 < 0$, Fig. 12 indicates that poles do not exist in the RIS. This explains the smoothly varying behavior of the parameters in Figs. 14a, 14b and 14c. Note that again for $\Delta a_1 < 0$ it is

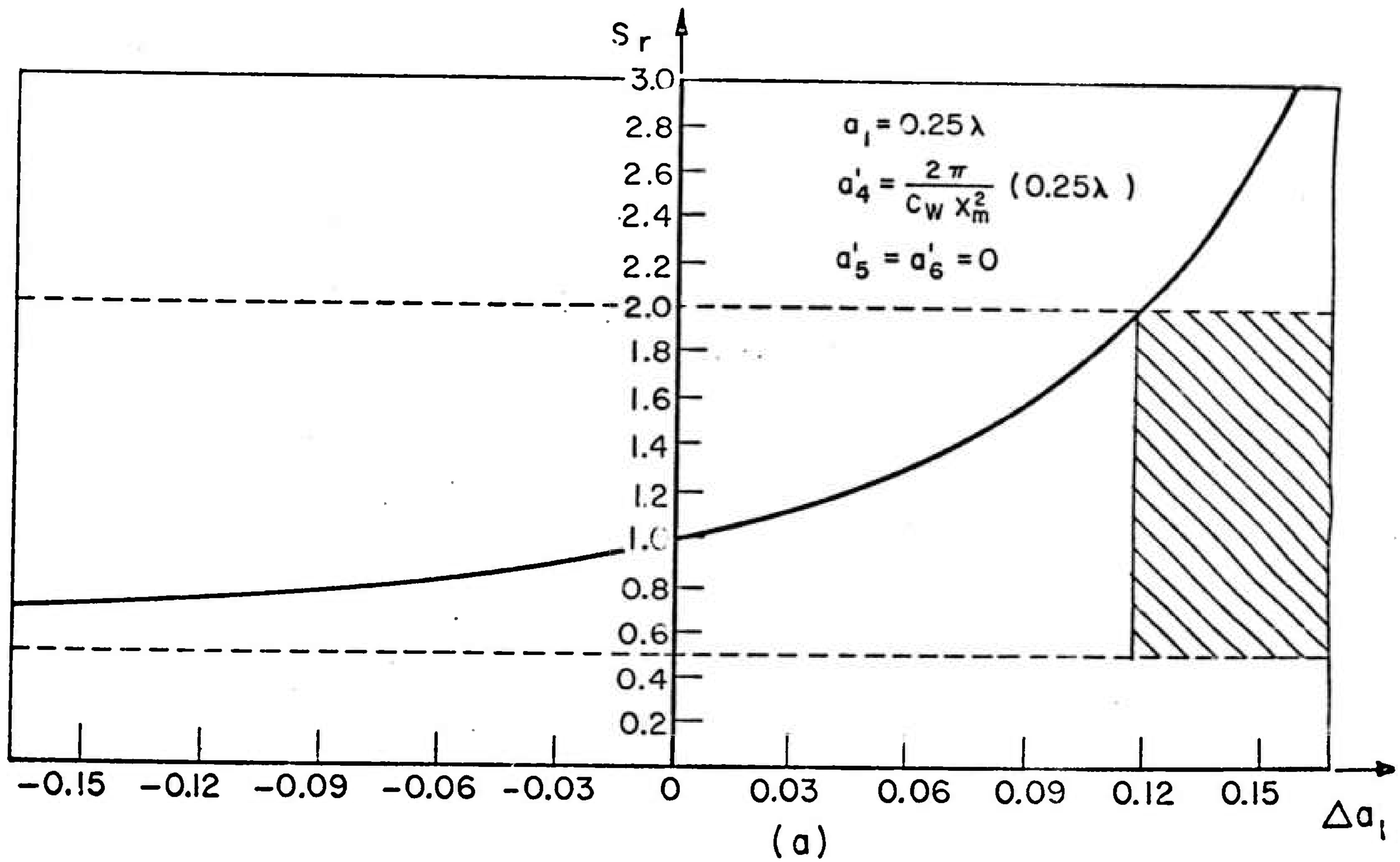

Fig. 13a. S_r versus Δa_1 for Case I.

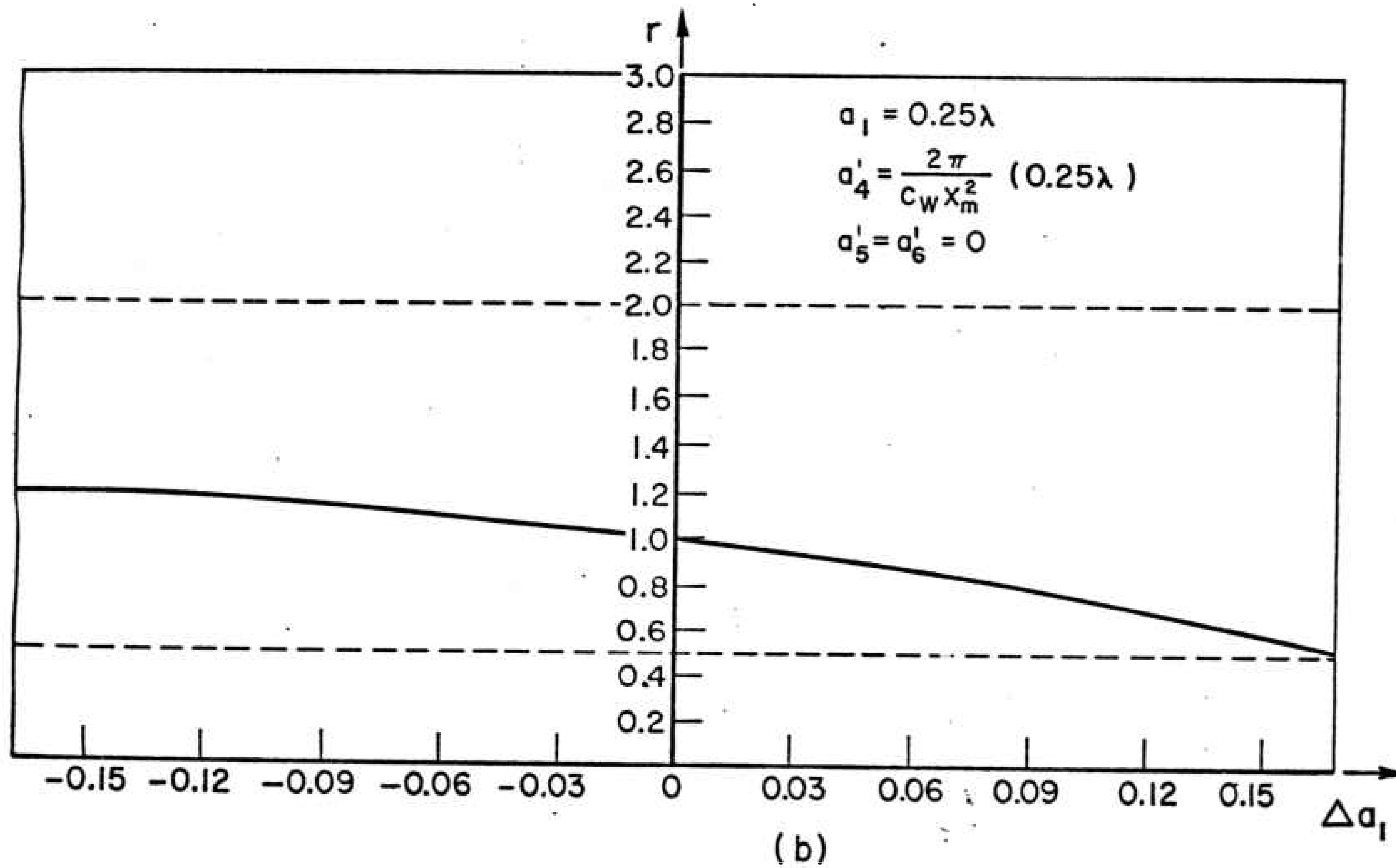

Fig. 13b. r versus Δa_1 for Case I.

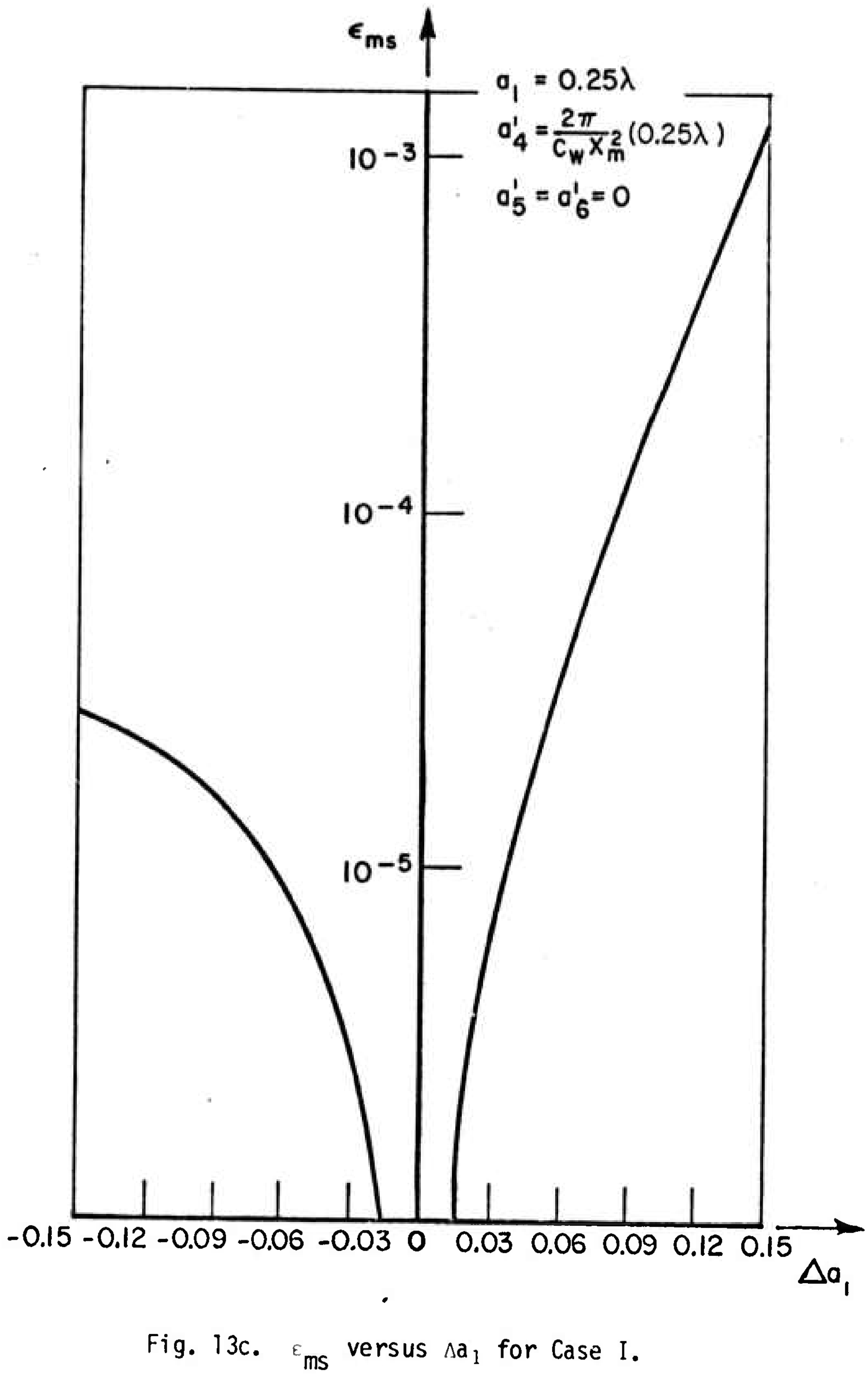

Fig. 13c. ϵ_{ms} versus Δa_1 for Case I.

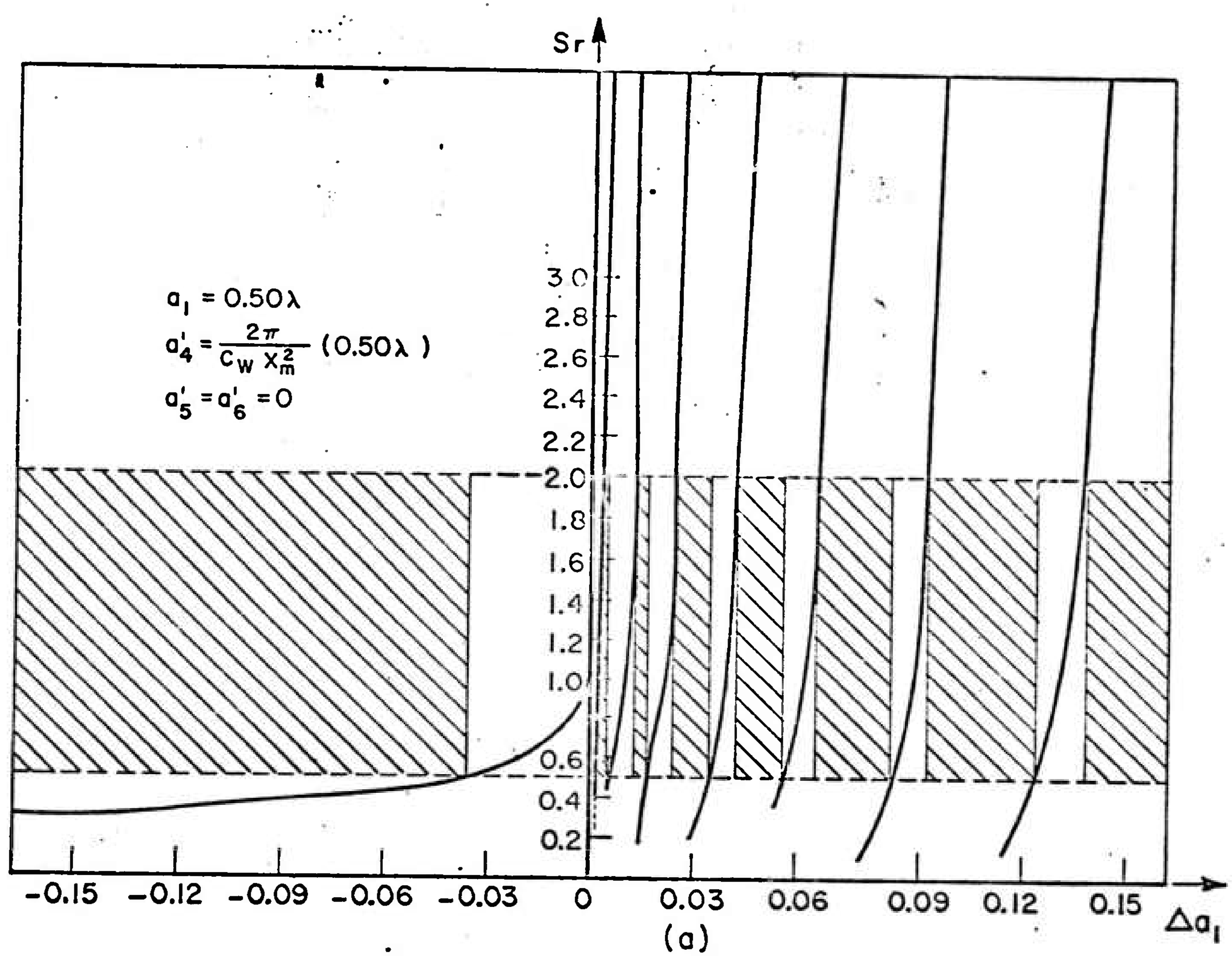

Fig. 14a. S_r versus Δa_1 for Case II.

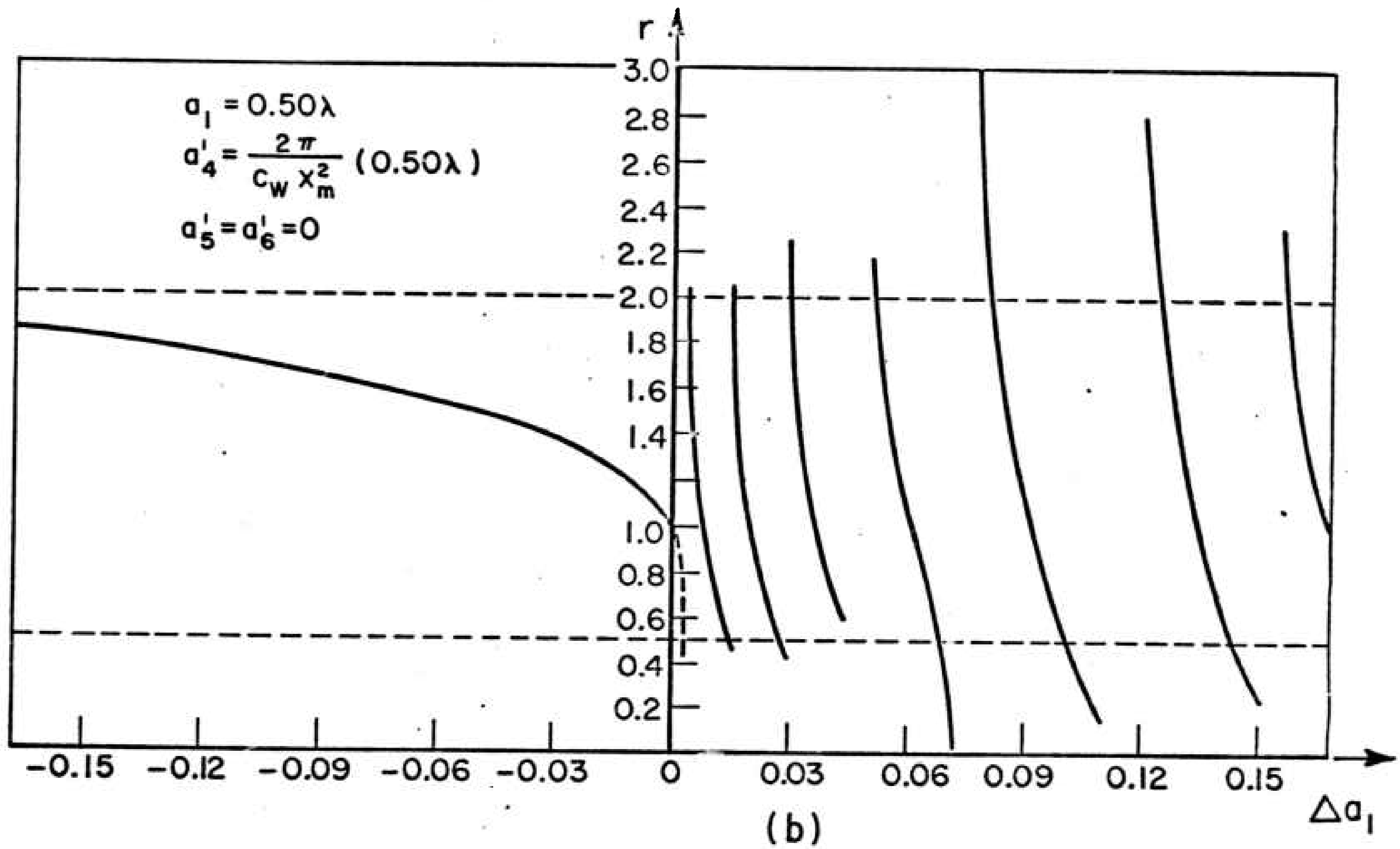

Fig. 14b. r versus Δa_1 for Case II.

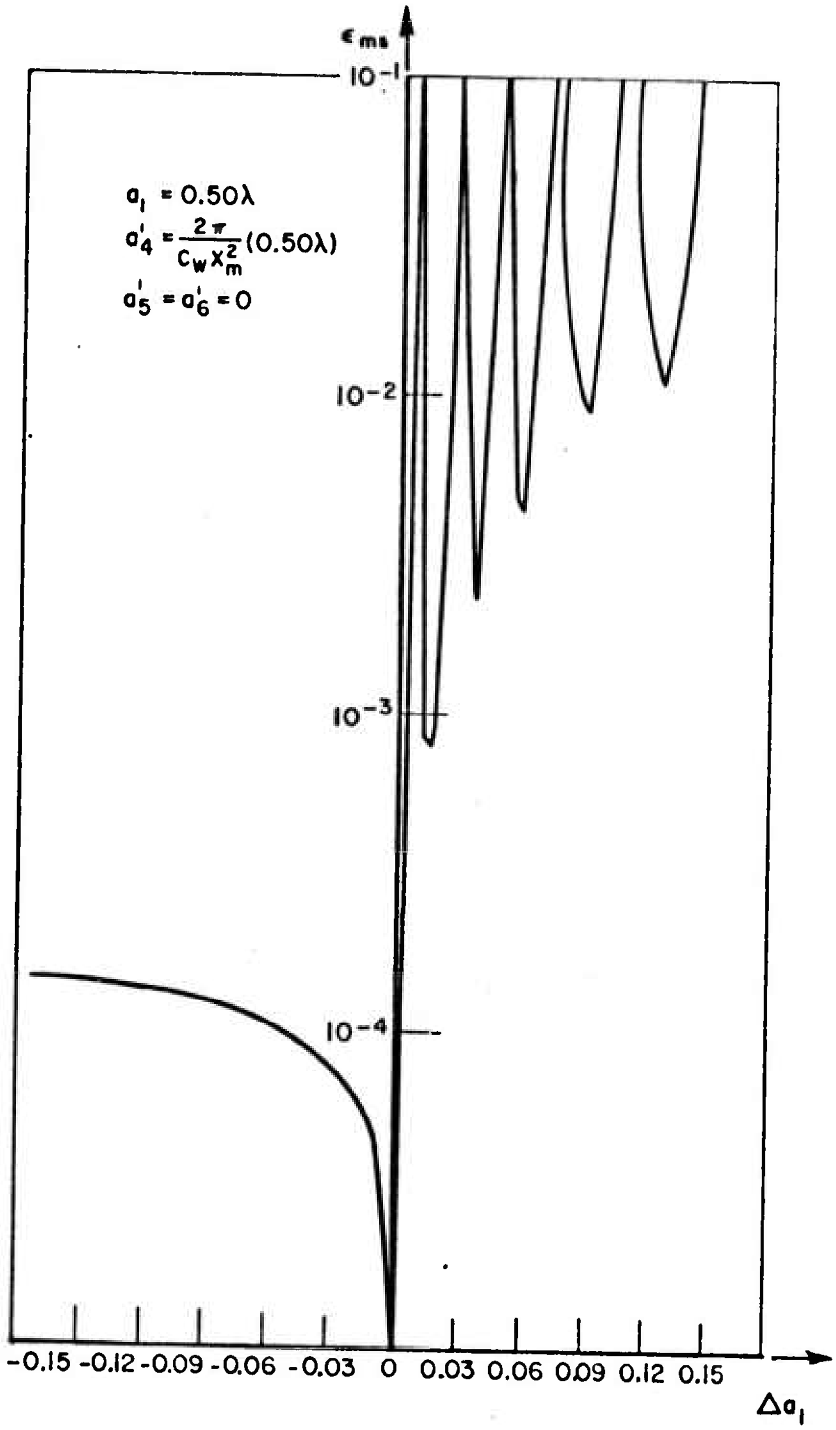

Fig. 14c. ϵ_{ms} versus Δa_1 for Case II.

the parameter Sr (see Fig. 14a) that establishes the restoration limit which occurs at $\Delta a_1 = -0.036\lambda$.

Thus for Case II, the limits on Δa_1 are a series of isolated small scale regions rather than large scale bounds present in Case I.

Now consider Figs. 15a, 15b and 15c. These graphs indicate that over the entire range of Δa_1 in Case III ($a_1 = 0.75\lambda$), there are only small scale regions in which the restoration parameters remain within the bounds defining a successfully restored image. Again, these regions are defined by the points where the parameter Sr exceeds its lower and upper bounds. However, the primary difference between the small scale regions in Cases II and III is their width, which is noticeably narrower in Case II (when $\Delta a_1 > 0$). Another basic difference between the two cases is the initial location of the poles within the RIS as seen in Fig. 12. In Case III, the poles are initially (i.e., when $\Delta a_1 = 0.0$) further removed from the point $|K_x| = K_m$.

The important consequence of the Case II and Case III studies is that the presence of RIS pole loci imposes limits on Δa_1, which in turn define a region of successful image restoration. These limits are a series of isolated small scale regions along the Δa_1 axis in Figs. 13a and 14a.

Next, an expression is derived that relates the presence of RIS pole loci to the magnitude of Sr. The restored Strehl ratio (Sr) is easily calculated if we remember that Sr is the spatial domain analog of the D.C. value in the frequency domain (see Chapter III, section E). That is, Sr is the average of the frequency components as defined in Eq.(72a).

$$\text{(72a)} \qquad Sr = \sum_{p=0}^{63} \sum_{q=0}^{63} R(p\,\Delta K_x, q\,\Delta K_y, a_1, 0, c_1, \Delta a_1, 0, \Delta c_1) \quad .$$

Substituting the discrete RIS (obtained by substituting Eqs. (34a) and (34b) into Eq. (58) with $a_1 = c_1$ and $\Delta a_1 = \Delta c_1$) into Eq. (72a) we obtain

$$\text{(72b)} \qquad Sr = 4\left[\sum_{p=0}^{31} \left(1 + \frac{\Delta a_1}{a_p}\right)\left(1 - \left\{(2\pi/K_m^2)(2K_m - |p\,\Delta K_x|)\,\Delta a_1 p\,\Delta K_x\right\}\right.\right.$$

$$\left.\left. \mathrm{Cot}\,(2\pi/K_m^2)(2K_m - |p\,\Delta K_x|)a_p\,p\,\Delta K_x\right]^2 \quad .$$

The terms under the summation sign in Eq. (72b) are graphed for Cases I, II and III in Figs. 16a, 16b and 16c, respectively. These graphs, which are the envelopes obtained by connecting the discrete frequency components, clearly indicate the presence of poles suggested in Fig. 12. Furthermore, the graphs suggest an important question. How is the value

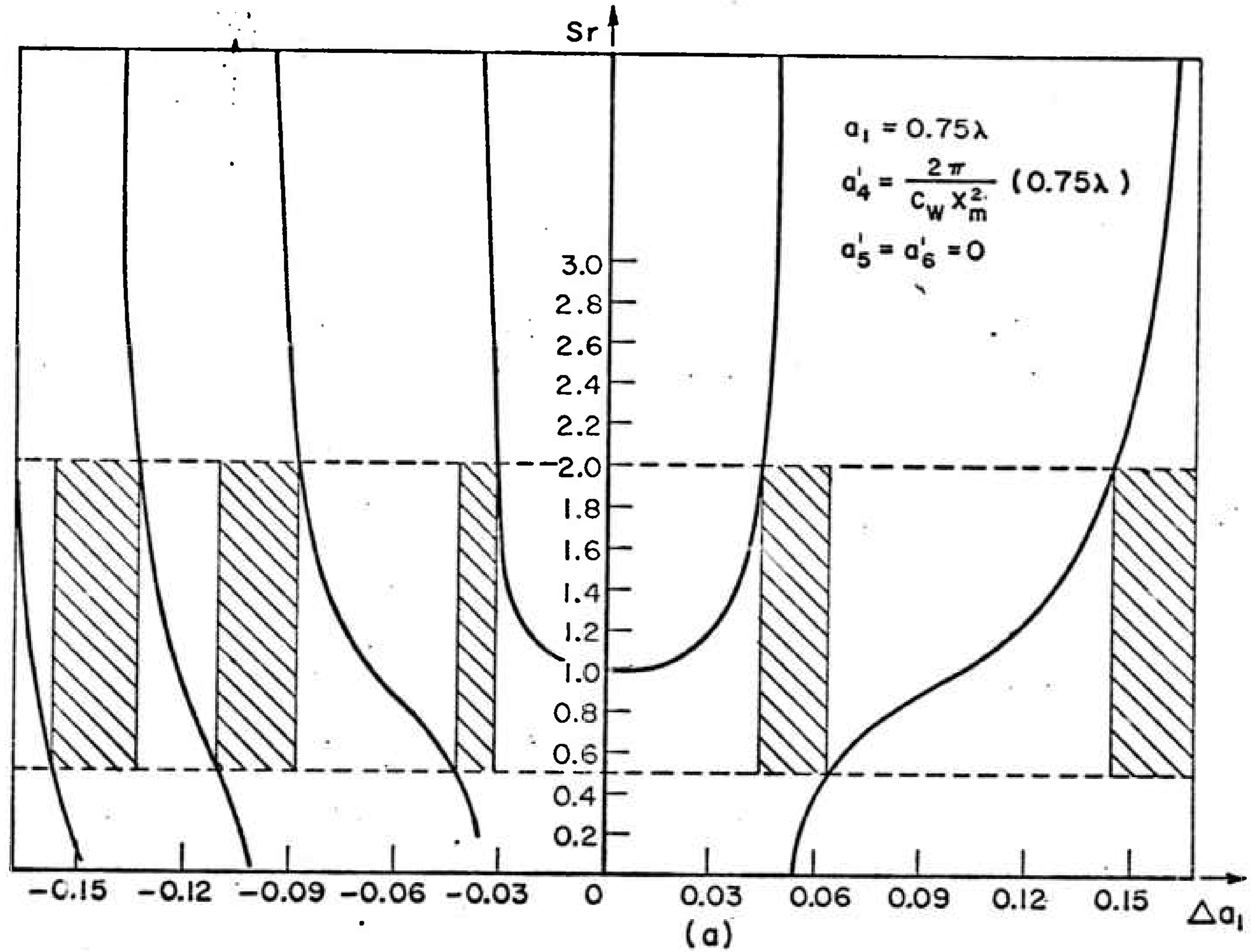

Fig. 15a. S_r versus Δa_1 for Case III.

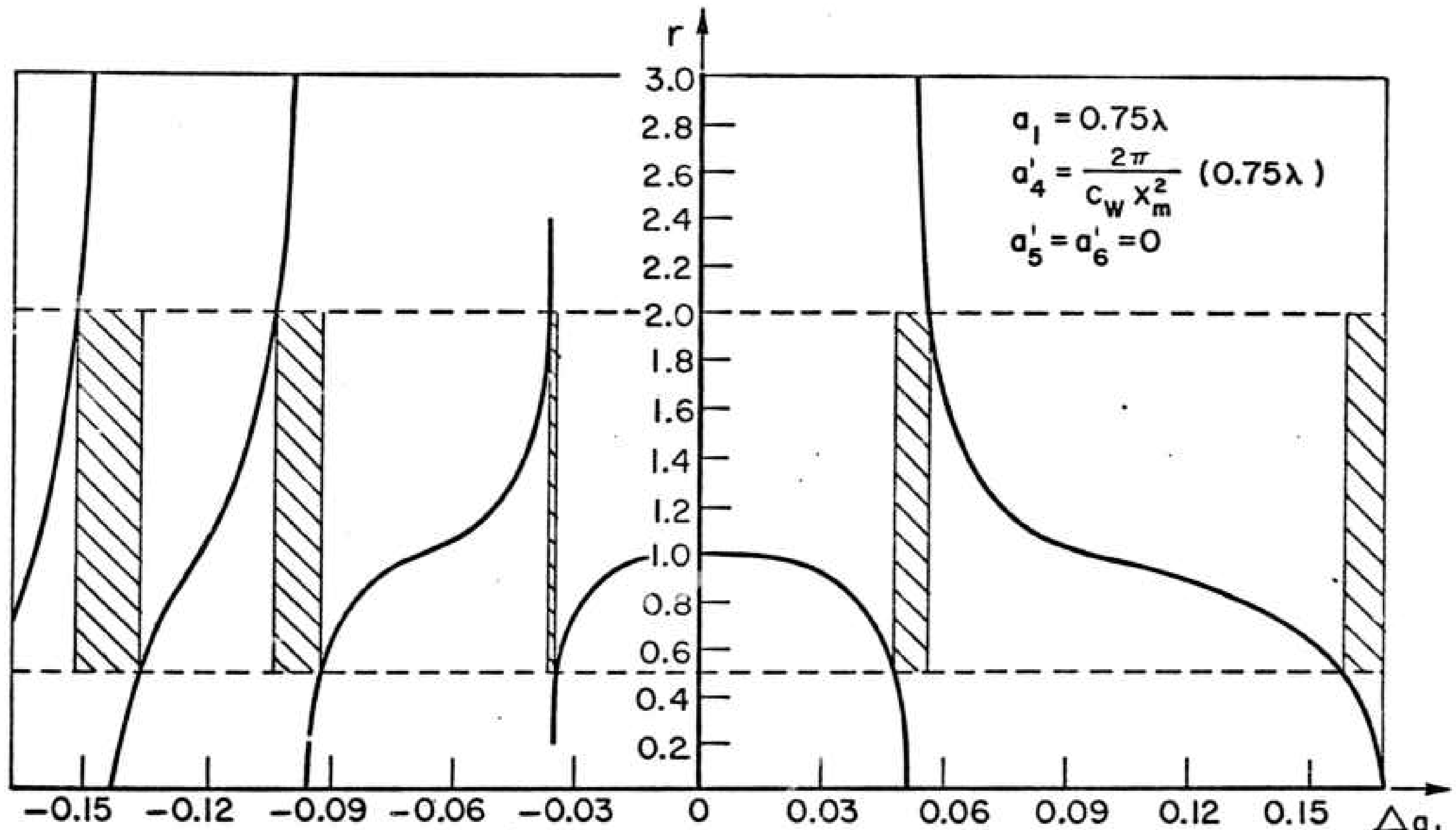

(b)

Fig. 15b. r versus Δa_1 for Case III.

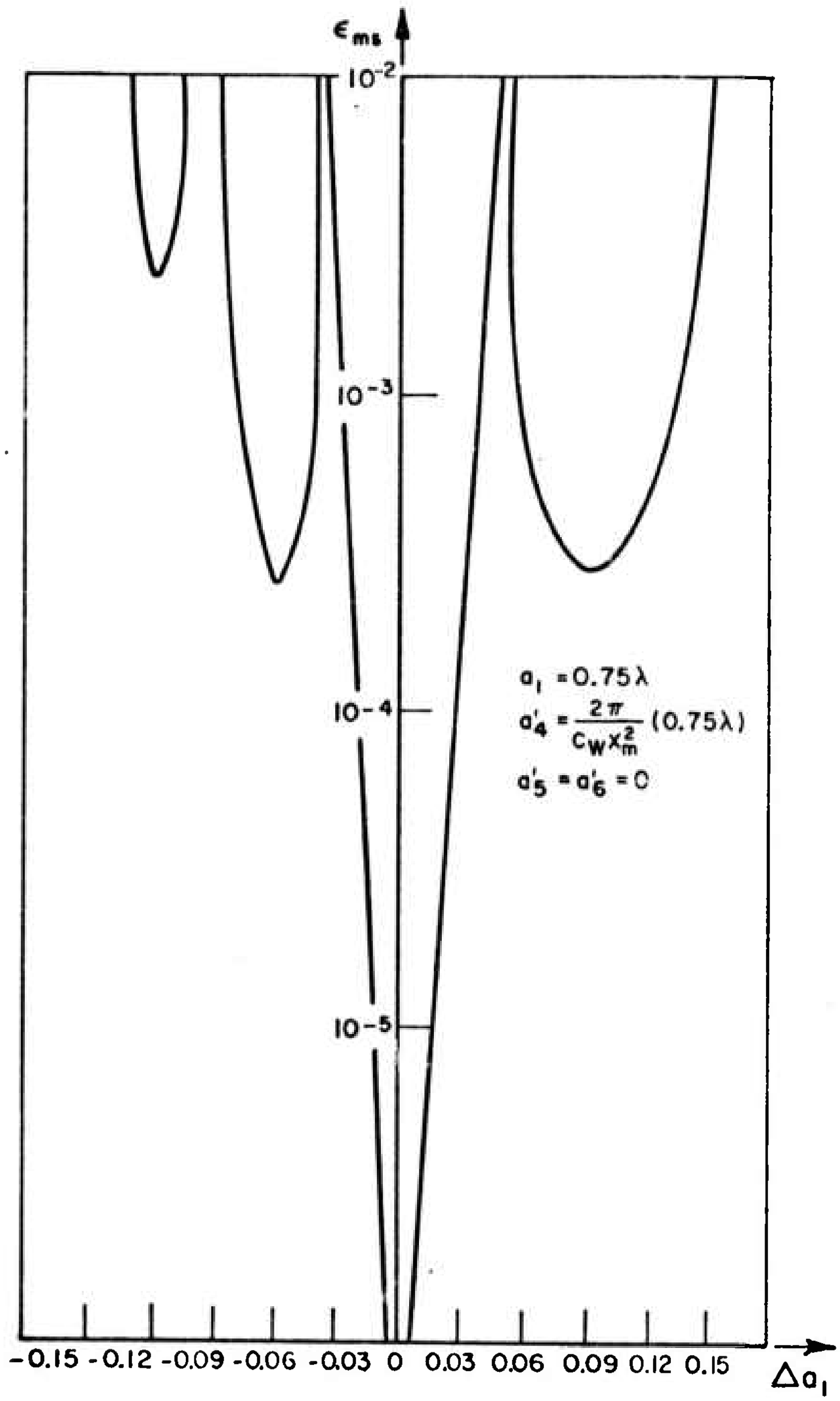

Fig. 15c. ϵ_{ms} versus Δa_1 for Case III.

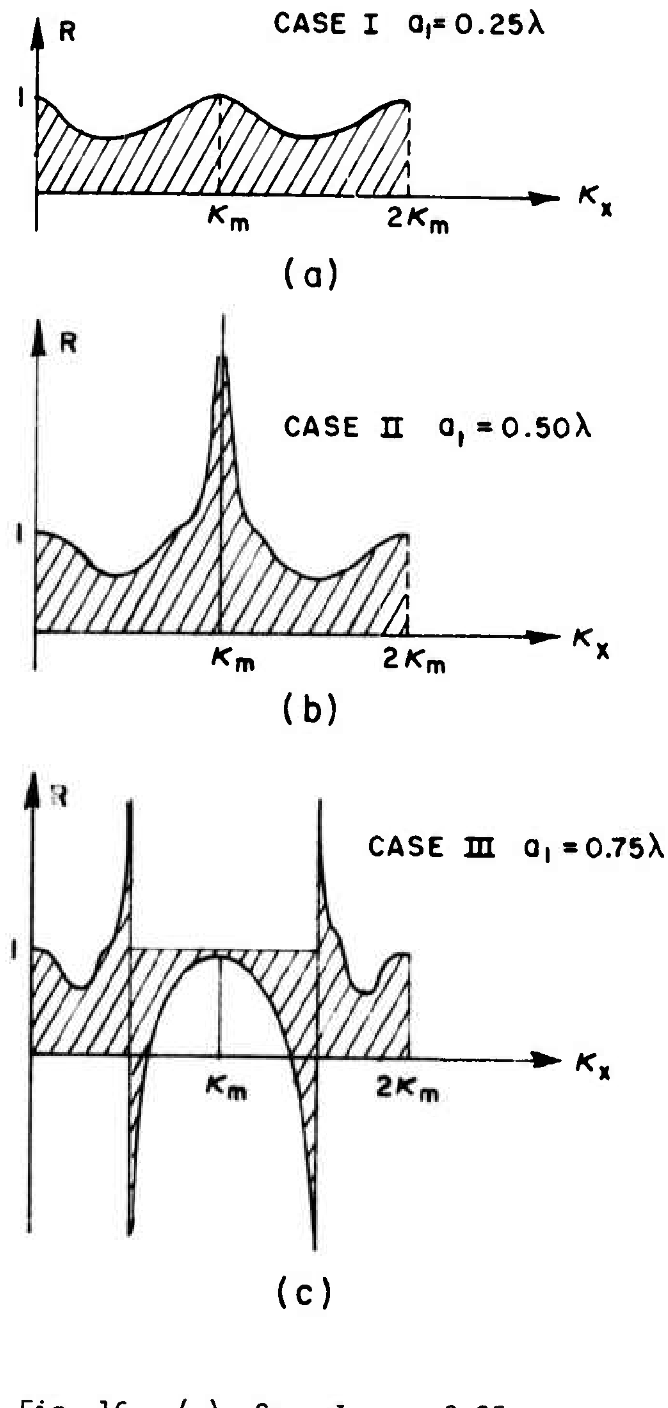

Fig. 16. (a) Case I $a_1 = 0.25\lambda$.
(b) Case II $a_1 = 0.50\lambda$.
(c) Case III $a_1 = 0.75\lambda$.

of Sr, which is calculated using Eq. (72b), affected by whether or not a pole exists exactly at a discrete frequency component? In order to answer this question, a relationship is derived to relate the magnitude of Sr to the possibility that a discrete RIS frequency component was evaluated at a pole.

The Cot argument $Z(K_x,K_y)$ taken from Eq. (72b) is graphed in Fig. 17a for Case II ($a_1 = 0.50\lambda$). A more detailed graph of this argument in the neighborhood of the point $K_x = K_m$ is presented in Fig. 17b. (Fig. 17b is exaggerated for clarity.)

Examining Fig. 17b, we see that when $\Delta a_1 = 0.0$, the Cot argument Z equals the value π at a point half way between the discrete frequency components 15 ΔK_x and 16 ΔK_x. Thus, since the ordinate of the discrete argument never actually equals the value π, the discrete RIS will not contain any true poles. Hence the parameter Sr, which is calculated from Eq. (72b), will be finite. However, referring to Fig. 17b, for the curve defined by $\Delta a_1 = \Delta a_1'$, the Cot argument Z does equal the value π at 15 ΔK_x and 16 ΔK_x ($K_m \pm \frac{1}{2}\Delta K_x$) and hence RIS poles do exist. For this situation, the summation over all frequency components will obviously exceed the limits imposed on Sr. When the value of a_p again increases to the value $a_1 + \Delta a_1''$ and then again to $a_1 + \Delta a_1'''$, the Cot argument behavior is analogous to that of $\Delta a_1 = 0$ and $\Delta a_1 = \Delta a_1'$, respectively. That is, poles do not exist in the RIS for $\Delta a_1 = \Delta a_1''$ but they do exist for $\Delta a_1 = \Delta a_1'''$. Thus, based on this analysis and the behavior of Sr exhibited in Figs. 13a, 14a and 15a, it seems natural to assume that small scale regions, in which scccessful image restoration occurs, will exist for values of Δa_1 in ranges similar to $\Delta a_1' \leq \Delta a_1 \leq \Delta a_1'''$ (see Fig. 17b). That is, successful restoration will exist in regions which are bounded at each end by Sr greatly exceeding its established limits. This assumption is verified in Fig. 18 which is a more detailed graph of Sr for Case II ($a_1 = 0.50\lambda$) where $\Delta a_1 > 0$. In this graph many small scale regions are apparent and each one is bounded by Sr greatly exceeding the limits Sr = 2.0 or Sr = 0.50.

The data for Fig. 18 was obtained by using the same computer processing techniques employed in Cases I, II and III but with finer resolution in the parameter Δa_1 (i.e., $\Delta a_1 = n0.001$, $n = 0,1,\cdots$).

Next, we show that indeed the small scale regions are bounded by those values of Δa_1 which result in the Cot argument Z equalling the value π at one or more discrete frequencies causing Sr to exceed the limits defining a successfully restored image. In order to prove this fact, an equation is derived that specifies the magnitude of Δa_1 required to shift a given ordinate value (π in this case) of the Cot argument p ΔK_x ($p = m/2$ m integer) units along the K_x axis (see Fig. 17b).

For the first step of this derivation we must recall that the continuous Cot argument (from Eq. (58)) is:

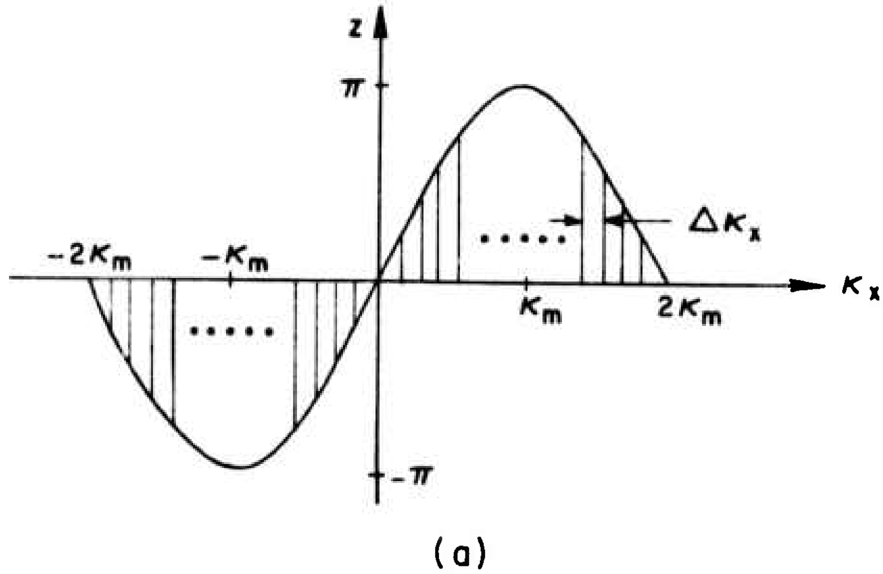

(a)

Fig. 17a. Graph of discrete Cot argument $Z(K_x,K_y)$.

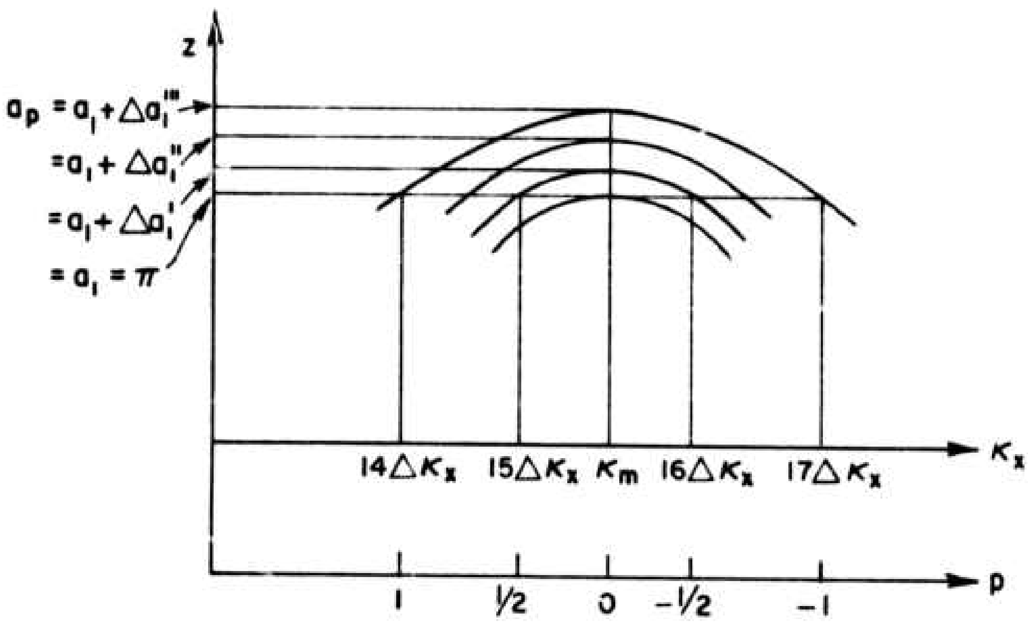

(b)

Fig. 17b. Graph of Z vs. Kx near the point $K_x = K_m$.

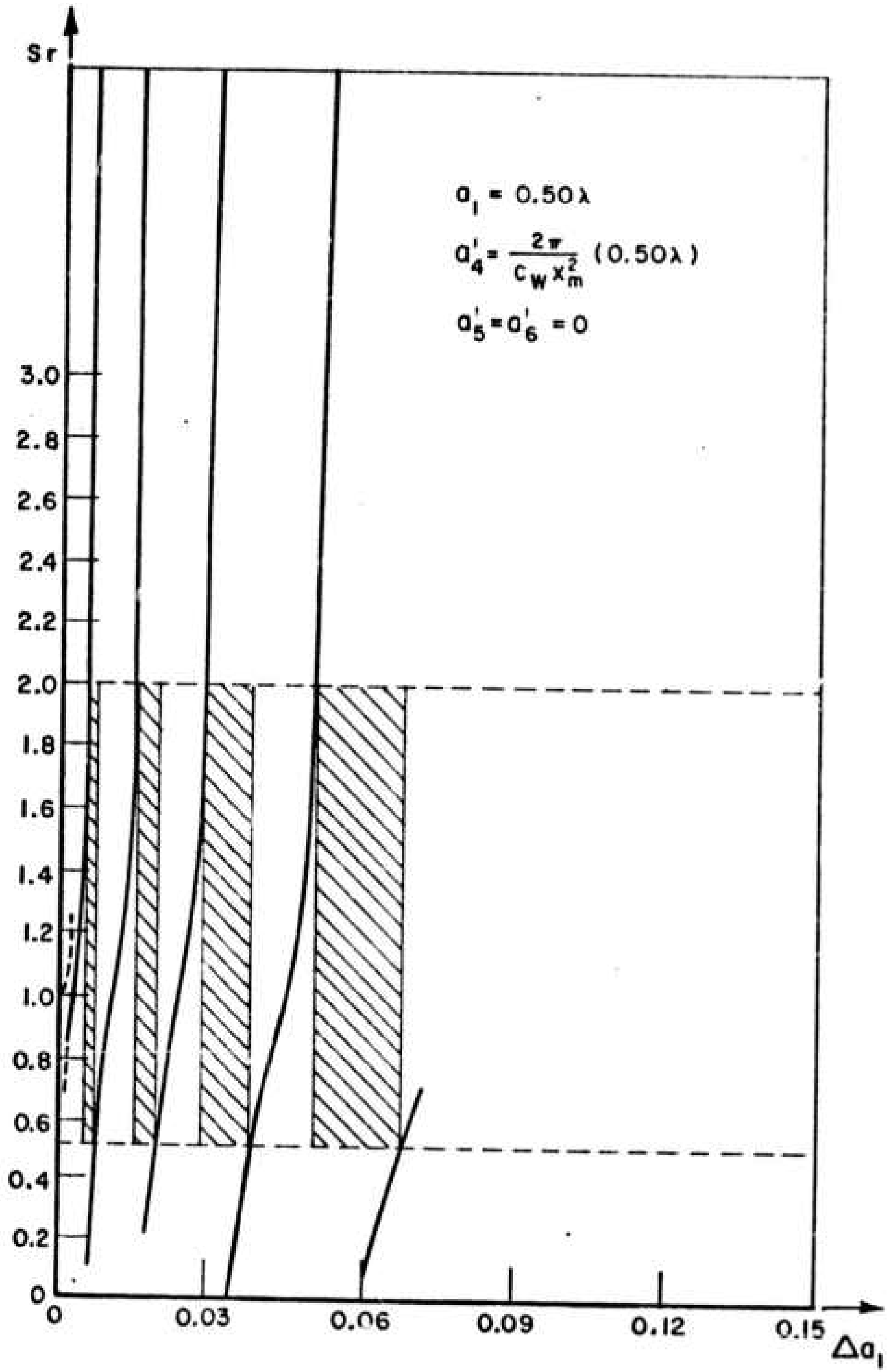

Fig. 18. Sr versus Δa_1 for Case II ($\Delta a_1 \geq 0$).

$$(73) \qquad Z = (2\pi/K_m^2)\, a_p(-K_x^2 + 2K_mK_x) \quad .$$

Rewriting Eq. (73) in terms of the discrete frequency components $K_x = n\,\Delta K_x$ and $K_m = 15\tfrac{1}{2}\,\Delta K_x$ (where n is an integer) we obtain:

$$(74) \qquad Z = (2\pi/240.25)\, a_p(-n^2 + 31n) \quad .$$

Eq. (74) is next expanded about the point $K_x = K_m$ by letting $|p\Delta K_x|$ ($p = m/2$, m = integer) measure distances along the abscissa with the point $K_x = K_m$ considered as the origin. Thus the Cot argument rewritten as a function of the variable p is:

$$(75) \qquad Z = (2\pi/240.25)\, a_p(240.25 - p^2).$$

Finally, substituting $a_p = a_1 + \Delta a_1$ and solving for Δa_1, the desired equation is obtained:

$$(76) \qquad \Delta a_1 = (Z/2\pi)\left(\frac{240.25}{240.25 - p^2}\right) - a_1 \quad .$$

Eq. (76) specifies the magnitude of Δa_1 required to shift the Cot argument Z, $p = m/2$ (m integer) units along the K_x axis.

Applying Eq. (76) to Case II, in which $a_1 = 0.50\lambda$ and $Z = \pi$ when $\Delta a_1 = 0.0$ (see Fig. 12), we have:

$$(77) \qquad \Delta a_1 = 0.50\left(\frac{p^2}{240.25 - p^2}\right) \quad .$$

Table 2 lists the values of Δa_1, calculated from Eq. (77), for $p = m/2$ ($m = 1,2,\cdots 17$). The values $p = m/2$ (m odd) correspond to those cases in which the Cot argument exactly equals the value π at one or more discrete frequency (see, for example, the $\Delta a_1 = \Delta a_1'$ curve in Fig. 17b) and poor image restoration is obtained. The values $p = m/2$ (m even) correspond to those cases in which the value π occurs exactly half way between two adjacent discrete frequencies (see, for example, the $\Delta a_1 = \Delta a_1''$ curve in Fig. 17b) and good image restoration is obtained.

Next, a series of computer processed images was generated using the same processing technique described earlier for Cases I, II and III; however, the values for Δa_1 were taken from Table 2. The values of Sr calculated for each restored image are graphed in Fig. 19a and 19b. Fig. 19a is a superposition of the data obtained from Table 2 over the

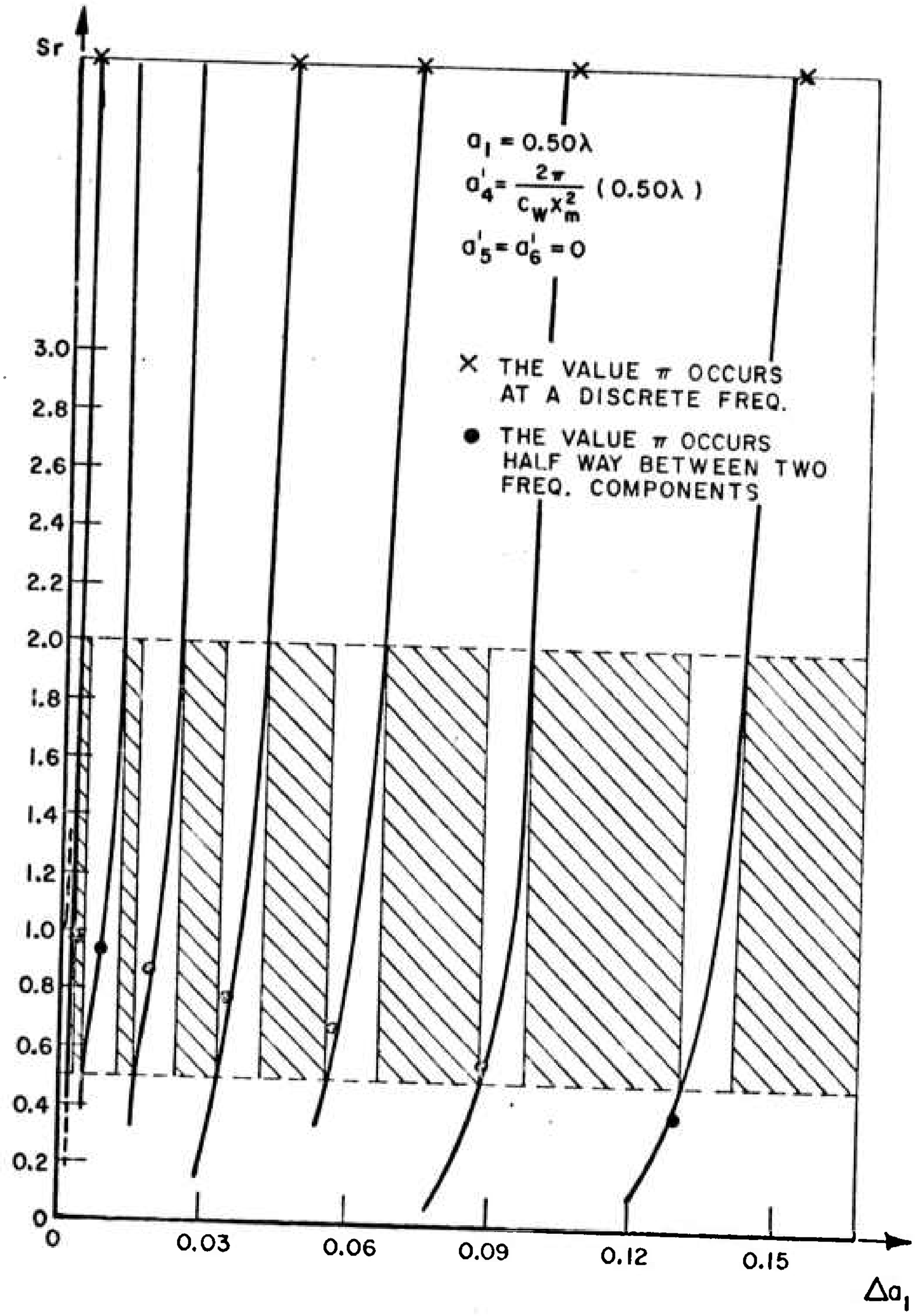

Fig. 19a. Sr evaluated at points listed in Table 2 and superimposed on Case II Sr versus Δa_1 graph.

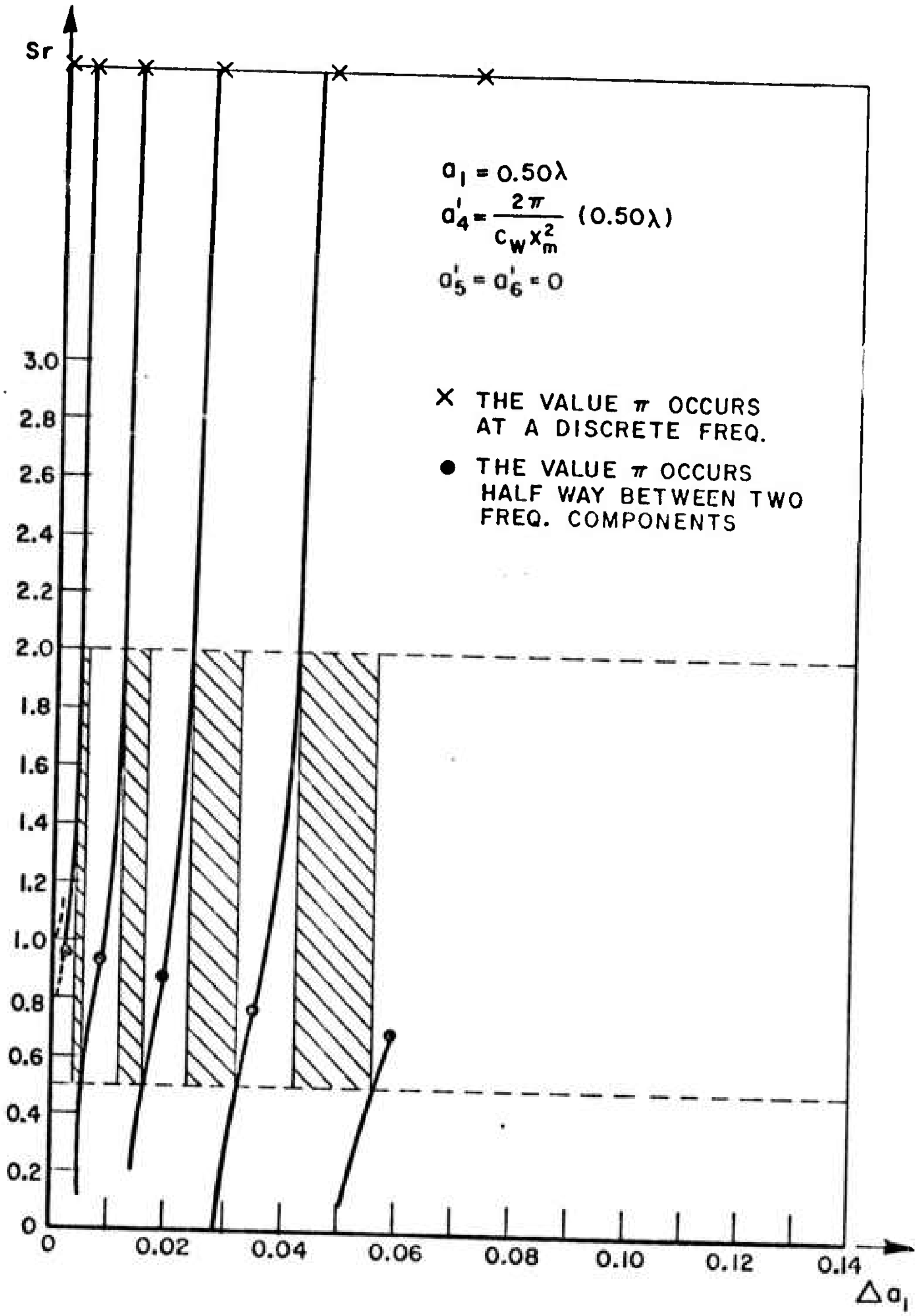

Fig. 19b. Sr evaluated at points listed in Table 2 and superimposed on Fig. 18.

TABLE 2

$a_1 = 0.50\lambda$	
$p = \frac{1}{2}$	$\Delta a_1 = 0.0005\lambda$
$= 1$	0.0021λ
$= 1\frac{1}{2}$	0.0047λ
$= 2$	0.0084λ
$= 2\frac{1}{2}$	0.0133λ
$= 3$	0.0194λ
$= 3\frac{1}{2}$	0.0268λ
$= 4$	0.0356λ
$= 4\frac{1}{2}$	0.0460λ
$= 5$	0.0580λ
$= 5\frac{1}{2}$	0.0720λ
$= 6$	0.0881λ
$= 6\frac{1}{2}$	0.1067λ
$= 7$	0.1281λ
$= 7\frac{1}{2}$	0.1528λ
$= 8$	0.1815λ
$= 8\frac{1}{2}$	0.2150λ

Case II results while Fig. 19b is a superposition of this data over the fine resolution Case II data (i.e., $\Delta a_1 = n0.001$ data). Note that when $p = m/2$ (m odd) the occurrence of the Cot π situation does indeed cause Sr to grossly exceed its upper bound. When $p = m/2$ (m even), the values of Sr are finite; in fact, in all but one case, shown in Fig. 19a, these values lie within the acceptable bounds for Sr defining a successfully restored image.

Finally, we derive an equation that expresses how rapidly the poles (i.e., points corresponding to $p = m/2$ where m is odd in the above analysis) migrate through the RIS as a function of Δa_1. This point is expressed by taking the derivative of the Cot argument Z with respect to Δa_1. The result of this calculation is:

$$\frac{\partial Z}{\partial \Delta a_1} = (2\pi/K_m^2)(2K_m - |K_x|)K_x \tag{78}$$

which is graphed in Fig. 20 as a function of K_x. Fig. 20 demonstrates that for a given perturbation Δa_1, the poles migrate from one discrete frequency component to the next adjacent component most rapidly (i.e., for the smallest change in Δa_1) when they occur near the point $K_x = K_m$. This fact corresponds exactly with the behavior seen in Case II ($a_1 = 0.50\lambda$) where rapid fluctuations occur in Sr as Δa_1 increase in magnitude (see Figs. 14a and 18). Fig. 20 also explains the behavior observed in Case III where Sr does not vary as rapidly as a function Δa_1. For Case III (Fig. 14a) when Δa_1 is positive, the poles migrate

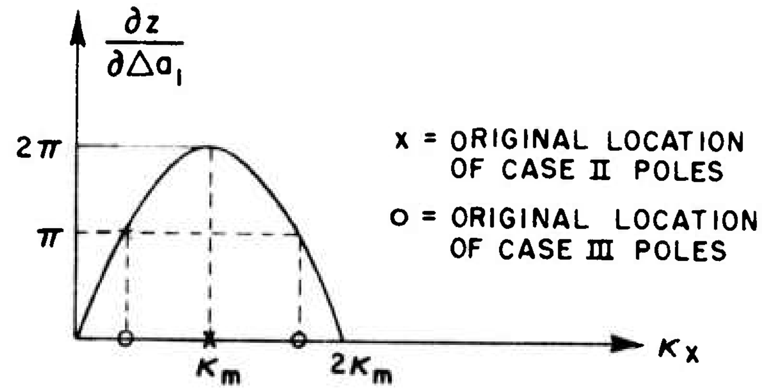

Fig. 20. Graph of $\frac{\partial Z}{\partial \Delta a_1}$ versus K_x.

farther away from the point $K_x = K_m$ and the small scale regions have larger separations; however, when Δa_1 is negative, the opposite effect is observed.

We can now generalize from these results. At best we can expect only small scale regions in which the imaging processing technique will produce a successfully restored image. In fact, from the data presented in Figs. 13a, 14a and 15a we can calculate the percentage of the Δa_1 range over which successful restoration results occur. For the three cases, these percentages are:

CASE I	85.5%
CASE II	14.0%
CASE III	71.0%

The presence of these small scale regions will obviously create great difficulties in the analysis of the restored images.

The fact that a particular image was not successfully restored could be the result of one of two factors. First, the object and point source could actually have been located in different isoplanatic patches. By definition of an isoplanatic patch (see Chapter I) we would expect poor quality restoration in this case. Second, the atmospheric effects which degraded the image might have created a situation in which the

Cot argument in the RIS assumed the value π at one or more discrete frequency components. As we have seen, this event will grossly perturb the RIS so that when it is inverse Fourier transformed, the restored image does not meet the restoration criterion established in Chapter III, section E.

C. Summary

This chapter has been devoted to the analysis of three cases of restored images. The three cases were defined by the values assumed for the wavefront parameter $a_1 (c_1 = a_1)$. Each case was analyzed for a series of perturbations $\Delta a_1 (\Delta c_1 = \Delta a_1)$ in the initial value for a_1. The restored image quality parameters, restored Strehl ratio (Sr), integral scale (r), and mean squared error (ε_{ms}) were calculated for each restored image, and then graphed as a function of Δa_1. From these graphs, the regions of successful image restoration are defined between the points at which Sr exceeds its upper and lower bounds. The exceedingly large values for Sr were then related to whether or not a pole was evaluated exactly at a discrete RIS frequency component.

Finally, it was demonstrated that the number of small scale regions for a given restoration range (i.e., range of a_p) is dependent on the initial location of the poles. For poles initially located near the point $K_x = K_m$, the poles migrate rapidly from one discrete RIS frequency component to the next adjacent frequency component. Thus, the regions of successful image restoration as a function of Δa_1 are very narrow (as small as 0.0005λ). For poles initially located at a distance from the point $K_x = K_m$, larger variations in Δa_1 are required to shift a pole from one discrete frequency to the next adjacent component. Thus, the regions of successful image restoration encompass a larger range of Δa_1.

The important point established in this chapter is that image restoration is a much more complex process than dividing a degraded image spectrum by a MTF and then inverse Fourier transforming to obtain the restored image. It has been shown that the poles introduced by this division operation limit image restoration to a series of small regions defining perturbations in the reference point wavefront that are not present in the point image wavefront.

CHAPTER V
REVIEW AND CONCLUSIONS

A. Review and Conclusions

This study has been devoted to the task of defining the limits for which the Fourier transform method of image restoration may be used to successfully restore turbulence degraded images obtained from a ground-based telescope.

In order to define the limits over which successful image restoration could occur, a turbulence degraded imaging system was modeled, with the assumption that the degrading effects could be expressed by expanding the E-field phase distribution across the telescope input aperture, in terms of a general second order quadratic equation. This expansion was used to define the degraded E field for a point object and the degraded E field from a reference point, which was assumed to be located in the transmitter plane with the point object. In order to model various reference point - object point separation, the reference point E-field phase distribution included a perturbation term in the quadratic phase coefficients.

The actual restored image analysis discussed in this study was based on a simplification of the general quadratic phase distribution discussed above. The specific case analyzed included only the spherical wavefront distortion in the E-field phase distributions. With the input aperture considered as a spatial frequency plane (see Chapter II-B), the object point and reference point E-field phase distributions for the spherical wavefront distortion case are, respectively:

(79a) $$E_a(K_x,K_y) = e^{j(d_i/k)^2\,(a_1K_x^2 + c_1K_y^2)}$$

(79b) $$E_a(K_x,K_y) = e^{j(d_i/k)^2\,\{(a_1 + \Delta a_1)K_x^2 + (c_1 + \Delta c_1)K_y^2\}}$$

The parameters a_1 and c_1 represent gross wavefront distortions while the parameters Δa_1 and Δc_1 define the phase perturbations resulting from the object point and reference point waves propagating through different turbulence conditions. (See Chapter II, section B and section C for details.)

Eqs. (79a) and (79b) were used as inputs for calculating the degraded image spectrum and the modulation transfer function (MTF), respectively. Then, using linear system theory, the restored image was obtained by calculating the inverse Fourier transform (The Fast Fourier Transform (FFT) was used for computer processing (see Appendix C) of the degraded image spectrum divided by the MTF or system transfer function.)

The restored image spectrum (RIS) obtained by dividing the degraded image spectrum by the MTF was subjected to a complete analysis. It was shown that the presence of poles (points at which the mathematical function takes on an infinitely large value) in the RIS definitely affected the restored image quality. Equations were derived that related the number and position, within the RIS, of these poles to the parameters $a_1 + \Delta a_1$ and $c_1 + \Delta c_1$.

The restored image quality was defined in terms of three restoration parameters: the restored Strehl ratio (Sr) which measures the peak image intensity, the integral scale (r) which measures image width, and the mean squared error (ε_{ms}) which are discussed in detail in Chapter III, section E. Limits were placed on these parameters which defined a successfully restored image.

A series of degraded images, generated using the model discussed above, was restored using a digital computer to implement the inverse Fourier transform restoration method. The degraded images were divided into three classes defined by the value assumed for the parameter $a_1 (= c_1)$. For each such class, a series of restorations were performed for perturbations $\Delta a_1 = n(0.006\lambda)$ $(n = \pm 0, 1, 2, \cdots 41)$.

The results of the analysis of these restored images, in terms of the restoration parameters, indicated that the presence of poles in the RIS did indeed cause the restored image to fail to meet the restored image quality criterion. It was determined that the quality parameter Sr was the most sensitive indicator of restored image quality, and hence this parameter was used to define the ranges of successful image restoration.

The conclusion drawn from this study was that a discrete RIS frequency component evaluated precisely at a pole was the major factor that caused Sr to greatly exceed its bounds indicating that the restored image failed to meet the quality criterion. As these poles migrated from one discrete spatial frequency component to the next adjacent discrete component, a region of successful image restoration was bounded. These small scale regions were found to be narrower in width (the width expressed in terms of Δa_1) when the poles originated near the spatial frequency spectrum midpoint $K_x = K_m$. Poles initially located some distance from this point $K_x = K_m$ were found to generate much wider small scale regions of successful image restoration.

For the three cases studied, it was shown that the sum of these small scale regions ranged from 14% to 85.5% of the processing range that was considered. Obviously, the 14.0% case indicates a very severe limit imposed on the Fourier transform image restoration method.

The results obtained from this study support the following six conclusions:

1. The major problem in the restoration of images is the presence of poles in the restored image spectrum (RIS).

2. The restored Strehl ratio (Sr) is the most sensitive of the three restoration parameters (integral scale, r, and mean squared error, ε_{ms}, are the other two restoration parameters) used to measure restored image quality.

3. The ability to successfully restore a degraded image does not monotonically decrease with increasing wavefront distortion but, rather, is oscillatory in nature.

4. Given a gross wavefront distortion, there may be many small ranges of wavefront perturbations in which successful image restoration occurs.

5. To assure restoration in the $a_1 = 0.50\lambda$ worst case considered here, Δa_1 must be less than or equal to 0.0005λ.

6. A probabilistic measure of successful image restoration as a function of gross wavefront distortion appears to be a useful discriptor.

B. Suggestions for Further Study

In this section, we propose suggestions for the possible extension of the work described in this study.

The next step beyond the work covered here might be that of employing a smoothing function such as a two-dimensional Gaussian or triangular function to smooth out the effects of poles present in the restored image spectrum (RIS) and hence improve the restored image quality. Further, this work suggests the need for investigating the validity of the discrete representation for the quotient of two functions as in calculating the RIS. The basic question to be answered is: do poles in the RIS result in effects such as a spatial domain analog to aliasing?

The other important extension would be that of including the cross term parameters b_1 and Δb_1 in the model for the degraded E-field wavefront. We would then be interested in the location of the new RIS pole loci and the effects of these poles on the size of the regions in which successful image restoration is obtained.

APPENDIX A
THE APERTURE PLANE CORRELATION FUNCTION

In this appendix we evaluate the convolution of our modeled E-field aperture distribution (Eq. (14)) with itself to find the aperture plane correlation function $C(K_x,K_y)$.

It was shown in Eq. (20) of Chapter II that the image plane intensity function and convolution of the field distribution over the telescope input aperture are Fourier transform mates. That is, from Eq. (20):

$$(20) \qquad I(x_2,y_2) \leftrightarrow (1/2\pi)^2 \iint_{-\infty}^{\infty} W(K_x - k_x, K_y - k_y)\, W^*(-k_x,-k_y)\, E_a(K_x - k_x, K_y - k_y)\, E_a^*(-k_x,-k_y)\, dk_x\, dk_y \quad .$$

In Eq. (20), K_x, K_y, k_x and k_y all are spatial frequencies in radian/mm and $W(K_x,K_y)$ is the aperture function defined by Eq. (19) as:

$$(19) \qquad W(K_x,K_y) = \begin{cases} 1 & \begin{array}{l} -K_m \le K_x \le K_m \\ -K_m \le K_y \le K_m \end{array} \\ 0 & \text{otherwise} \end{cases} \quad .$$

By letting $k_x = -k_x$ and $k_y = -k_y$ and multiplying Eq. (20) by $(2\pi)^2$, we have shown in Eq. (21) that:

$$(21) \qquad I_i(x_2,y_2) = (2\pi)^2 I(x_2,y_2) \leftrightarrow C(K_x,K_y) =$$

$$\iint_{-\infty}^{\infty} W(K_x+k_x,K_y+k_y)\, W^*(k_x,k_y)\, E_a(K_x+k_x,K_y+k_y)\, E_a^*(k_x,k_y)\, dk_x\, dk_y$$

where $C(K_x,K_y)$ is the aperture plane correlation function.

We now are interested in evaluating Eq. (21) for the case where the input field distribution is given by Eq. (14) as:

$$(14) \qquad E_a(K_x,K_y) = e^{j\,(d_i/k)^2 (aK_x^2 + bK_xK_y + cK_y^2)} \quad .$$

Substituting Eq. (14) into Eq. (21), we obtain Eq. (23) which is the actual integral that we must evaluate.

$$C(K_x,K_y) = e^{j(d_i/k)^2(aK_x^2 + bK_xK_y + cK_y^2)} \iint_{-\infty}^{\infty} W(K_x+k_x,K_y+k_y)\, W^*(k_x,k_y)\, e^{j(d_i/k)^2\left[(2aK_x + bK_y)k_x + (2cK_y + bK_x)k_y\right]}\, dk_x\, dk_y \quad . \tag{23}$$

Since the aperture function restricts the input field at $\pm K_m$, we can determine the limits of integration by considering the correlation of the two aperture functions. Fig. A1, below, shows the two aperture functions involved in the K_x correlation.

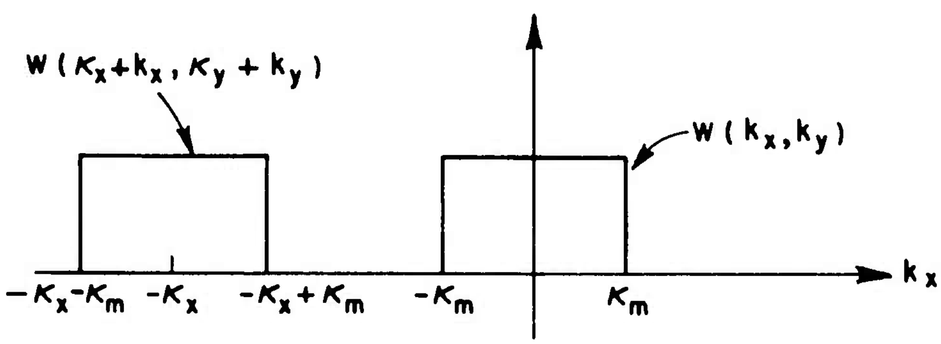

Fig. A1.

The complex conjugate notation (*) may be dropped from $W^*(k_x,k_y)$ since the aperture function is a real function. Using Fig. A1 to define the limits of integration, we find that when $K_x \geq 0$, the limits on k_x are

$$-K_m \leq k_x \leq -K_x + K_m \tag{A1a}$$

and when $K_x \leq 0$, the limits on it are

$$-K_x-K_m \leq k_x \leq K_m \quad . \tag{A1b}$$

Since the input aperture is square, the same results apply for the K_y correlation. That is, the k_y integration limits are defined

(A2a) for $K_y \geq 0$, as $-K_m \leq k_y \leq -K_y + K_m$ and

(A2b) for $K_y \leq 0$, as $-K_y - K_m < k_y \leq K_m$.

Thus, Eq. (23) can be rewritten as the product of a k_x and a k_y integration. Each integration is then divided into two parts defined by Eqs. (A1) and (A2). Note that the aperture function can be dropped since its effect is now reflected in the limits of integration. Thus, we have:

(A3)
$$C(K_x,K_y) = e^{j(d_i/k)^2(aK_x^2 + bK_xK_y + cK_y^2)}$$
$$\left\{\int_{-K_m}^{-K_x+K_m} e^{j(d_i/k)^2(2aK_x+bK_y)k_x}\, dk_x + \int_{-K_x-K_m}^{K_m} e^{j(d_i/k)^2(2aK_x+bK_y)k_x}\, dk_x\right\}$$
$$\left\{\int_{-K_m}^{-K_y+K_m} e^{j(d_i/k)^2(2cK_y+bK_x)k_y}\, dk_y + \int_{-K_y-K_m}^{K_m} e^{j(d_i/k)^2(2cK_y+bK_x)k_y}\, dk_y\right\}$$

Remember that the first term inside each bracket is defined for K_x or $K_y \geq 0$, and the second term is defined for K_x or $K_y < 0$.

Since the two bracketed terms in Eq. (A3) have exactly the same mathematical form, only the first one will be calculated here. The second will follow exactly the same steps.

For the first term, when $K_x \geq 0$, we have:

(A4)
$$\int_{-K_m}^{-K_x+K_m} e^{j(d_i/k)^2(2aK_x+bK_y)k_x}\, dk_x = \left.\frac{e^{j(d_i/k)^2(2aK_x+bK_y)}}{j(d_i/k)^2(2aK_x+bK_y)}\right|_{-K_m}^{-K_x+K_m}$$
$$= \frac{e^{j(d_i/k)^2(2aK_x+bK_y)(-K_x+K_m)} - e^{j(d_i/k)^2(2aK_x+bK_y)K_m}}{j(d_i/k)^2(2aK_x+bK_y)}$$

$$= \frac{e^{j(d_i/k)^2 \frac{1}{2}(2aK_x+bK_y)K_x}}{\frac{1}{2}(d_i/k)^2(2aK_x+bK_y)2j}\left[e^{j(d_i/k)^2(2aK_x+bK_y)(K_m-\frac{1}{2}K_x)} - e^{-j(d_i/k)^2(2aK_x+bK_y)(K_m-\frac{1}{2}K_x)}\right].$$

This last equality in Eq. (A4) can be written in terms of the Sin function as:

$$\text{(A6)} \qquad \int_{-K_m}^{-K_x+K_m} e^{j(d_i/k)^2(2aK_x+bK_y)k_x}\, dk_x =$$

$$e^{-j(d_i/k)^2 \frac{1}{2}(2aK_x+bK_y)K_x}\; \frac{\mathrm{Sin}(d_i/k)^2(2aK_x+bK_y)(K_m-\frac{1}{2}K_x)}{\frac{1}{2}(d_i/k)^2(2aK_x+bK_y)}.$$

For the second K_x term in Eq. (A3) we have for $K_x \le 0$:

$$\text{(A7)} \qquad \int_{-K_x-K_m}^{K_m} e^{j(2aK_x+bK_y)k_x}\, dk_x = \left.\frac{e^{j(2aK_x+bK_y)k_x}}{j(2aK_x+bK_y)}\right|_{-K_x-K_m}^{K_m}$$

$$= \frac{e^{j(d_i/k)^2(2aK_x+bK_y)K_m} - e^{-j(d_i/k)^2(2aK_x+bK_y)(K_m+K_x)}}{j(d_i/k)^2(2aK_x+bK_y)}$$

$$= \frac{e^{-j(d_i/k)^2 \frac{1}{2}(2aK_x+bK_y)K_x}}{\frac{1}{2}(d_i/k)^2(2aK_x+bK_y)2j}\left[e^{j(d_i/k)^2(2aK_x+bK_y)(K_m+\frac{1}{2}K_x)} - e^{-j(d_i/k)^2(2aK_x+bK_y)(K_m+\frac{1}{2}K_x)}\right].$$

Again, this last equality in Eq. (A7) can be written in terms of a Sin function as:

(A8) $$\int_{-K_m}^{-K_x+K_m} e^{j(d_i/k)^2(2aK_x+bK_y)k_x}\, dk_x =$$

$$e^{-j(d_i/k)^2\frac{1}{2}(2aK_x+bK_y)K_x}\left[\frac{\mathrm{Sin}(d_i/k)^2(2aK_x+bK_y)(K_m+\frac{1}{2}K_x)}{\frac{1}{2}(d_i/k)^2(2aK_x+bK_y)}\right] .$$

Thus for the K_x correlation we have from Eqs. (A6) and (A8) that:

(A9) $$\int_{-K_m}^{-K_x+K_m} e^{j(d_i/k)^2(2aK_x+bK_y)k_x} dk_x + \int_{-K_x-K_m}^{K_m} e^{j(d_i/k)^2(2aK_x+bK_y)k_x} dk_x$$

$$= e^{j(d_i/k)^2\frac{1}{2}(2aK_x+bK_y)K_x}\left\{\left[\frac{\mathrm{Sin}(d_i/k)^2(2aK_x+bK_y)\frac{1}{2}(2K_m-K_x)}{\frac{1}{2}(d_i/k)^2(2aK_x+bK_y)}\right]\right.$$

$$\left. + \frac{\mathrm{Sin}(d_i/k)^2(2aK_x+bK_y)\frac{1}{2}(2K_m+K_x)}{\frac{1}{2}(d_i/k)^2(2aK_x+bK_y)}\right\} .$$

We next multiply the first Sin term (defined for $K_x \geq 0$) by $(2K_m-K_x)/(2K_m-K_x)$ and the second Sin term (defined for $K_x \leq 0$) by $(2K_m+K_x)/(2K_m+K_x)$ which casts these terms in the form of the familiar Sin x/x or Sinc function. Thus the right-hand side of Eq. (A9) becomes:

$$\text{(A10)} \quad = e^{j(d_i/k)^2\frac{1}{2}(2aK_x+bK_y)K_x} \left\{ (2K_m-K_x) \frac{\text{Sin}(d_i/k)^2(2aK_x+bK_y)\frac{1}{2}(2K_m-K_x)}{(d_i/k)^2(2aK_x+bK_y)\frac{1}{2}(2K_m-K_x)} \right.$$

$$\left. + (2K_m+K_x) \frac{\text{Sin}(d_i/k)^2(2aK_x+bK_y)\frac{1}{2}(2K_m+K_x)}{(d_i/k)^2(2aK_x+bK_y)\frac{1}{2}(2K_m+K_x)} \right\} .$$

Eq. (A10) may be written in a more compact form by employing $|K_x|$ and remembering that the first term in Eq. (A10) is defined for $K_x \geq 0$ and the second term is defined for $K_x \leq 0$.

$$\text{(A11)} \quad = e^{j(d_i/k)^2\frac{1}{2}(2aK_x+bK_y)K_x} \; (2K_m-|K_x|)$$

$$\frac{\text{Sin}\,(d_i/k)^2(2aK_x+bK_y)\frac{1}{2}(2K_m-|K_x|)}{(d_i/k)^2(2aK_x+bK_y)\frac{1}{2}(2K_m-|K_x|)} .$$

We next obtain the solution to the second bracketed term in Eq. (A3) by substituting:

K_x for K_y
K_y for K_x
c for a

into Eq. (A11) to obtain:

$$\text{(A12)} \quad = e^{j(d_i/k)^2\frac{1}{2}(2cK_y+bK_x)K_y} \; (2K_m-|K_y|) \frac{\text{Sin}(d_i/k)^2(2cK_y+bK_x)\frac{1}{2}(2K_m-|K_y|)}{(d_i/k)^2(2cK_y+bK_x)\frac{1}{2}(2K_m-|K_y|)}$$

Substituting Eq. (A11) and (A12) into Eq. (A3), we see that the multiplicative phase term is cancelled leaving us with:

$$\text{(A13)} \quad C(K_x,K_y) = (2K_m-|K_x|) \frac{\text{Sin}(d_i/k)^2(2aK_x+bK_y)\frac{1}{2}(2K_m-|K_x|)}{(d_i/k)^2(2aK_x+bK_y)\frac{1}{2}(2K_m-|K_x|)}$$

$$(2K_m-|K_y|) \frac{\text{Sin}(d_i/k)^2(2cK_y+bK_x)\frac{1}{2}(2K_m-|K_y|)}{(d_i/k)^2(2cK_y+bK_x)\frac{1}{2}(2K_m-|K_y|)} .$$

Eq. (A13) which is defined for:

$$(A14) \qquad -2K_m \leq K_x \leq 2K_m$$
$$-2K_m \leq K_y \leq 2K_m$$

is the desired result and is used in Eq. (24) of Chapter I.

APPENDIX B
CALCULATION OF THE RESTORED IMAGE SPECTRUM

In this appendix, we calculate the restored image spectrum (RIS) $I_R(K_x,K_y)$ given in Chapter II, Eq. (29), from the degraded image spectrum $C(K_x,K_y)$ (aperture plane correlation function) and the system modulation transfer function (MTF) $H(K_x,K_y)$.

$$(29) \qquad I_R(K_x,K_y) = \frac{C(K_x,K_y)}{H(K_x,K_y)}$$

The formulas for $C(K_x,K_y)$ and $H(K_x,K_y)$ are given in Chapter II, Eqs. (24) and (28), respectively. The following derivation of the RIS will involve only the Sinc terms multiplied by $(2K_m-|K_x|)$ in Eqs. (24) and (28). The second Sinc term multiplied by $(2K_m-|K_y|)$ is obtained directly from the following derivation by making the substitutions:

(B1a) $\quad K_y$ for K_x

and

(B1b) $\quad c_1$ for a_1

and

(B1c) $\quad \Delta c_1$ for Δa_1 .

Substituting these Sinc terms into Eq. (29), we have as one term in the RIS:

$$(B2) \qquad \frac{\dfrac{\mathrm{Sin}\left\{(d_i/k)^2(2aK_x+bK_y)\tfrac{1}{2}(2K_m-|K_x|)\right\}}{(d_i/k)^2(2aK_x+bK_y)\tfrac{1}{2}(2K_m-|K_x|)}}{\dfrac{\mathrm{Sin}\left\{(d_i/k)^2\left[2(a+\Delta a)K_x+(b+\Delta b)K_y\right]\tfrac{1}{2}(2K_m-|K_x|)\right\}}{(d_i/k)^2\left[2(a+\Delta a)K_x+(b+\Delta b)K_y\right]\tfrac{1}{2}(2K_m-|K_x|)}}$$

Next, by substituting a_1, Δa_1, b_1 and Δb_1 obtained from Eqs. (15a) and (15b) and remembering that $(d_i/k)^2(2\pi/x_m^2) = 2\pi/K_m^2$, we express Eq. (B2) as a ratio of two Sin functions multiplied by a factor involving K_x and K_y.

(B3) $$\left[1 + \frac{2\Delta a_1 K_x + \Delta b_1 K_y}{2a_1 K_x + b_1 K_y}\right] \cdot$$

$$\frac{\sin\left\{(2\pi/K_m^2)(2a_1K_x+b_1K_y)\frac{1}{2}(2K_m-|K_x|)\right\}}{\sin\left\{(2\pi/K_m^2)\left[2(a_1+\Delta a_1)K_x+(b_1+\Delta b_1)K_y\right]\frac{1}{2}(2K_m-|K_x|)\right\}} \quad .$$

We next add and subtract:

(B4) $$\Delta Y = (2\pi/K_m^2)(2\Delta a_1 K_x + \Delta b_1 K_y)\frac{1}{2}(2K_m-|K_x|)$$

from the argument of the Sin function in the numerator of Eq. (B3) which we define as:

(B5) $$Y = (2\pi/K_m^2)(2a_1K_x + b_1K_y)\frac{1}{2}(2K_m-|K_x|) \quad .$$

Thus, Eq. (B3) becomes:

$$\left[1 + \frac{2\Delta a_1 K_x + \Delta b_1 K_y}{2a_1 K_x + b_1 K_y}\right] \frac{\sin(Y+\Delta Y - \Delta Y)}{\sin(Y+\Delta Y)} \quad .$$

Applying the trigonometry identity,

$$\sin A\text{-}B = \sin A \cos B - \cos A \sin B \quad ,$$

to Eq. (B5), we have:

(B6) $$\left[1 + \frac{2\Delta a_1 K_x + \Delta b_1 K_y}{2a_1 K_x + b_1 K_y}\right] \frac{\sin(Y+\Delta Y)\cos\Delta Y - \cos(Y+\Delta Y)\sin(\Delta Y)}{\sin(Y+\Delta Y)}$$

which simplifies to:

(B7) $$\left[1 + \frac{2\Delta a_1 K_x + \Delta b_1 K_y}{2a_1 K_x + b_1 K_y}\right] \cos\Delta Y - \sin\Delta Y \cot(Y+\Delta Y) \quad .$$

Substituting Eqs. (B4) and (B5) into (B7), we have:

(B8)
$$\left[1 + \frac{2\Delta a_1K_x + \Delta b_1K_y}{2a_1K_x + b_1K_y}\right]$$

$$\left[\mathrm{Cos}\left\{(2\pi/K_m^2)(2\Delta a_1K_x - \Delta b_1K_y)\tfrac{1}{2}(2K_m-|K_x|)\right\} - \right.$$

$$\mathrm{Sin}\left\{(2\pi/K_m^2)(2\Delta a_1K_x - \Delta b_1K_y)\tfrac{1}{2}(2K_m-|K_x|)\right\}$$

$$\left. \cdot\,\mathrm{Cot}\left\{(2\pi/K_m^2)\left[2(a_1+\Delta a_1)K_x + (b_1+\Delta b_1)K_y\right]\tfrac{1}{2}(2K_m-|K_x|)\right\}\right]$$

As stated earlier, the second term in the RIS is obtained by making the substitutions indicated in Eqs. (B1a), (B1b) and (B1c) into Eq. (B8) to yield:

(B9)
$$\left[1 + \frac{2\Delta c_1K_y + \Delta b_1K_x}{2c_1K_y + b_1K_x}\right]$$

$$\left[\mathrm{Cos}\left\{(2\pi/K_m^2)(2\Delta c_1K_y - \Delta b_1K_x)\tfrac{1}{2}(2K_m-|K_y|)\right\} - \right.$$

$$\mathrm{Sin}\left\{(2\pi/K_m^2)(2\Delta c_1K_y - \Delta b_1K_x)\tfrac{1}{2}(2K_m-|K_y|)\right\}$$

$$\left. \cdot\,\mathrm{Cot}\left\{(2\pi/K_m^2)\left[2(a_1+\Delta c_1)K_y - (b_1+\Delta b_1)K_x\right]\tfrac{1}{2}(2K_m-|K_y|)\right\}\right].$$

The desired RIS, $R(K_x,K_y,a_1,b_1,c_1,\Delta a_1,\Delta b_1,\Delta c_1)$, in Eq. (31) of Chapter II is the product of Eqs. (B8) and (B9).

(B10)
$$R(K_x,K_y,a_1,b_1,c_1,\Delta a_1,\Delta b_1,\Delta c_1) = \left[1 + \frac{2\Delta a_1K_x + \Delta b_1K_y}{2a_1K_x + \Delta b_1K_y}\right]$$

$$\left[\mathrm{Cos}\left\{(2\pi/K_m^2)(2\Delta a_1K_x - \Delta b_1K_y)\tfrac{1}{2}(2K_m-|K_x|)\right\} - \mathrm{Sin}\left\{(2\pi/K_m^2)\right.\right.$$

$$\left.\cdot\,(2\Delta a_1K_x - \Delta b_1K_y)\tfrac{1}{2}(2K_m-|K_x|)\right\}\mathrm{Cot}\left\{(2\pi/K_m^2)\left[2(a_1+\Delta a_1)K_x - (b_1+\Delta b_1)K_y\right]\right.$$

$$\left.\left.\cdot\,\tfrac{1}{2}(2K_m-|K_x|)\right\}\right]\left[1 + \frac{2\Delta c_1K_y + \Delta b_1K_x}{2c_1K_y + b_1K_x}\right]\left[\mathrm{Cos}\left\{(2\pi/K_m^2)(2\Delta c_1K_y - \Delta b_1K_x)\right.\right.$$

$$\cdot \tfrac{1}{2}(2K_m - |K_y|)\Big\} - \mathrm{Sin}\Big\{(2\pi/K_m^2)(2\Delta c_1 K_y - \Delta b_1 K_x)\tfrac{1}{2}(2K_m - |K_y|)\Big\}$$

$$\cdot \mathrm{Cot}\Big\{(2\pi/K_m^2)\big[2(a_1+\Delta a_1)K_y - (b_1+\Delta b_1)K_x\big]\tfrac{1}{2}(2K_m - |K_y|)\Big\}\Big] \quad .$$

The above equation is the desired result used in Chapter II, Eq. (31).

APPENDIX C
THE FAST FOURIER TRANSFORM (FFT)

In this appendix we discuss pertinent aspects of the Fast Fourier Transform (FFT) algorithm and the Discrete Fourier Transform (DFT) from which it is derived. Attention is also given to both frequency and spatial domain discrete variables and their relationships with the spatial domain sampling rate.

It is a well known fact that for a frequency band-limited system, the time waveform is exactly described by a Discrete Fourier Series (DFS), when the time function is sampled at a rate greater than or equal to the highest frequency component in the pass band. This relationship applies equally for a n-dimensional system. The Discrete Fourier Transform (DFT) applied to the DFS is a bi-directional mapping operation with mathematical properties analogous to those of the Fourier integral. The Fast Fourier Transform (FFT) is a method for efficiently computing the DFT of a n-dimensional series of discrete data samples. For the purpose of this study, we restrict our attention to the two-dimensional FFT. The FFT takes advantage of the fact that the coefficients for the DFT may be calculated by using a parallel iterative technique rather than the coefficient-by-coefficient direct approach. For a two-dimensional array of dimension N by N, where $N = 2^m$ (m integer), direct calculation of the DFT coefficients requires N^4 arithmetic operations; however, the FFT, using the iterative technique, requires only $4N^2\log_2 N = 4N^2 m$ arithmetic operations [18]. When N = 64, as in this study, the FFT requires only $4m/N^2 = 24/4096$ or 0.6% of the possible N^4 arithmetic operations, and hence computer time, required by the direct method. Not only does the FFT reduce the required computer time by 99.4%, but it reduces the computer round off errors by the same factor [18].

The defining equation for the DFT is:

$$\text{(C1)} \qquad \tilde{I}_{IJ} = \sum_{R=1}^{Nx} \sum_{S=1}^{Ny} I_{RS}\, e^{-j2\pi\left(\frac{(I-1)(R-1)}{Nx} + \frac{(J-1)(S-1)}{Ny}\right)}$$

where I_{RS} is an Nx by Ny array of discrete data samples and $\tilde{I}_{IJ}$, the DFT of I_{RS}, is an Nx by Ny array of discrete frequency components. The inverse DFT is given by:

$$\text{(C2)} \qquad I_{RS} = \frac{1}{N_x N_y} \sum_{I=1}^{Nx} \sum_{J=1}^{Ny} \tilde{I}_{IJ}\, e^{j2\pi\left(\frac{(I-1)(R-1)}{Nx} + \frac{(J-1)(S-1)}{Ny}\right)} .$$

The validity of this transform pair can be easily verified by substituting $\tilde{I}_{IJ}$ from Eq. (C1) into Eq. (C2) and using the orthogonal relationship for exponentials, which is:

$$\text{(C3)} \quad \sum_{I=1}^{Nx} \sum_{J=1}^{Ny} e^{-j2\pi\left(\frac{(I-1)(R-1)}{Nx} + \frac{(J-1)(S-1)}{Ny}\right)} e^{j2\pi\left(\frac{(I-1)(M-1)}{Nx} + \frac{(J-1)(N-1)}{Ny}\right)}$$

$$= \begin{cases} Nx\ Ny & \text{for} \quad R = M \\ & \qquad\ \ S = N \\ 0 & \text{otherwise} \end{cases} \quad .$$

For convenience, the DFT transform pair is represented by the shorthand notation:

$$\text{(C4)} \qquad I_{RS} \leftrightarrow \tilde{I}_{IJ} \quad .$$

We are assuming in this study that the frequency spectrum is band-limited at $K_x = \pm 2K_m$ and $K_y = \pm 2K_m$ (see Eq. (21)); thus the sample spacing $\Delta x = \Delta y$ in the spatial plane must be given by:

$$\text{(C5)} \qquad \Delta x = \Delta y < \tfrac{1}{2}(2\pi/2K_m) = (\pi/2K_m) \quad .$$

We further assume that the width, W, of spatial function equals an integral number of samples; that is:

$$\text{(C6)} \qquad W = Nx\Delta x = Ny\Delta y = \frac{Nx\pi}{2K_m} = \frac{Ny\pi}{2K_m} \quad .$$

Substituting $Nx = W/\Delta x$ and $Ny = W/\Delta y$ into Eq. (C1) and (C2) and grouping terms in the exponents, we have:

$$\text{(C7)} \qquad \tilde{I}_{IJ} = \sum_{R=1}^{Nx} \sum_{S=1}^{Ny} I_{RS}\, e^{-j2\pi\left(\frac{(I-1)}{W}(R-1)\Delta x + \frac{(J-1)}{W}(S-1)\Delta y\right)}$$

and

$$\text{(C8)} \qquad I_{RS} = \frac{1}{N_x N_y} \sum_{I=1}^{Nx} \sum_{J=1}^{Ny} \tilde{I}_{IJ}\, e^{j2\pi\left(\frac{(I-1)}{W}(R-1)\Delta x + \frac{(J-1)}{W}(S-1)\Delta y\right)} \quad .$$

From Eq. (C7), we see that $\tilde{I}_{IJ}$ is periodic with period $1/\Delta x$ along the K_x axis and $1/\Delta y$ along the K_y axis; that is:

$$\text{(C9)} \qquad \tilde{I}_{IJ} = \tilde{I}_{I \pm n/\Delta x, J \pm n/\Delta y} \qquad \text{(n integer)} \quad .$$

Also, we see that the sample spacing in the frequency plane is:

$$\text{(C10)} \qquad \Delta K_x = \Delta K_y = 1/W \quad .$$

From Eq. (C8), we find that I_{RS} is periodic with period W along the x and y axes; that is:

$$\text{(C11)} \qquad I_{RS} = I_{R \pm nW, S \pm nW} \qquad \text{(n integer)} \quad .$$

The sample spacing has already been specified as $\Delta x = \Delta y$. Further, note that since the spatial domain period $W = Nx\Delta x = Ny\Delta y$ (from Eq. (C6)) and the frequency plane periods $1/\Delta x = Nx/W$ and $1/\Delta y = Ny/W$ (from Eq. (C6) are both directly proportional to Nx and Ny, $\tilde{I}_{IJ}$ and I_{RS} are also periodic with periods Nx and Ny. Thus, each array of Nx by Ny number represents one cycle of the periodic frequency and spatial domain functions.

These results are summarized in Fig. C1 for the one-dimensional case (i.e., $\tilde{I}_I \leftrightarrow I_R$), which simplifies the graphic presentation.

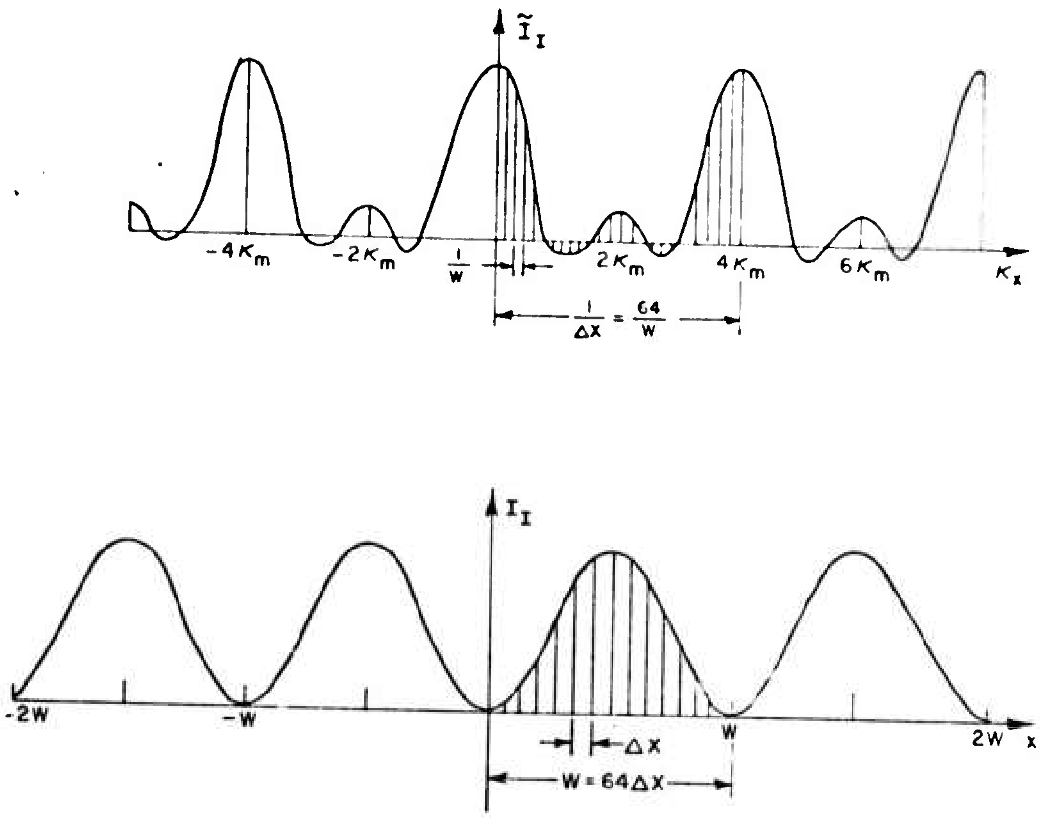

Fig. C1. Discrete Fourier transform.

REFERENCES

1. Tatarski, V. I., "Wave Propagation in a Turbulent Medium," Dover Publications Inc., New York, N.Y.

2. Tatarski, V. I., "The Effects of the Turbulent Atmosphere on Wave Propagation," U.S. Department of Commerce National Technical Information Service, Springfield, Va.

3. Goodman, Joseph W., "Introduction to Fourier Optics," McGraw-Hill Book Company, San Francisco, California.

4. Gaskill, Jack D., Imaging Through a Randomly Inhomogeneous Medium by Wavefront Reconstruction, J. Opt. Soc. Am. 58, pp. 600-608.

5. Goodman, J. W., et al, Holographic Imagery Through Atmospheric Inhomogeneities, Proc. NASA/ERC Seminar (Cambridge, Mass., Dec. 1968).

6. Frieden, B. Roy, "Restoring with Maximum Likelihood," Technical Report 67, University of Arizona, February 1971.

7. Mueller, Peter F. and Reynolds, George O., Image Restoration by Removal of Random-Media Degradations, J. Opt. Soc. Am. 57, pp. 1338-1344.

8. MacAdam, David Pearce, Digital Image Restoration by Constrained Deconvolution, J. Opt. Soc. Am. 60, pp. 1617-1627.

9. Harris, James L., Sr., Image Evaluation and Restoration, J. Opt. Soc. Am., 56, pp. 569-574.

10. McGlamery, Benjamin L., Restoration of Turbulence-Degraded Images, J. Opt. Soc. Am. 57, pp. 293-297.

11. Huang, Thomas S., et al, Image Processing, Proc. of the IEEE, 59, pp. 1586-1609.

12. Andrews, Henry C., N Topics in Search of an Editorial: Heuristics, Supperresolution, and Bibliography, Proc. of the IEEE, 60, pp. 891-894.

13. Sawchuk, Alexander A., Space-Variant Image Motion Degradation and Restoration, Proc. of the IEEE, 60, pp. 854-861.

14. Fried, David L., Statistics of a Geometric Representation of Wavefront Distortion, J. Opt. Soc. Am., 55, p. 1427.

15. Collins, Stuart A. Jr., "Investigation of Laser Propagation Phenomena," (Technical Report), Report 3432-4, March 1973, The Ohio State University ElectroScience Laboratory, Department of Electrical Engineering.

16. Linfoot, E. H., J. Opt. Soc. Am., 46, p. 740.

17. Barry, J. E., Final Report, Project 700D, Mitre Corp., Bedford, Massachusetts, August 1971.

18. Cochran, William T., et al, What is the Fast Fourier Transform?, IEEE Trans. on Audio and Electroacoustics, AU-15, pp. 45-55.